










RESEARCH ARTICLE

10.1029/2022GC010822

Gas Emissions and Subsurface Architecture of Fault-Controlled Geothermal Systems: A Case Study of the North Abaya Geothermal Area

Key Points:

- First conceptual model of a fault-controlled magmatic geothermal resource in the East African Rift
- Focus on North Abaya in the Main Ethiopian Rift and show that deep hydrothermal upflow is concentrated along a major graben bounding fault
- Magmatic CO₂ emissions along this fault are ~300 t d⁻¹ and comparable to average values from the world's subaerial volcanoes

William Hutchison¹ , Euan R. D. Ogilvie¹, Yafet G. Birhane² , Peter H. Barry³ , Tobias P. Fischer⁴ , Chris J. Ballentine⁵ , Darren J. Hillemonds⁵, Juliet Biggs⁶ , Fabien Albino^{6,7} , Chelsea Cervantes⁸, and Snorri Guðbrandsson⁸

¹School of Earth and Environmental Sciences, University of St Andrews, St Andrews, UK, ²School of Earth Sciences, University of Addis Ababa, Addis Ababa, Ethiopia, ³Woods Hole Oceanographic Institution, Woods Hole, MA, USA, ⁴Department of Earth and Planetary Sciences, University of New Mexico, Albuquerque, NM, USA, ⁵Department of Earth Sciences, University of Oxford, Oxford, UK, ⁶COMET, School of Earth Sciences, University of Bristol, Bristol, UK, ⁷CNRS, IRD, Université Grenoble Alpes, Université Savoie Mont Blanc, Université Gustave Eiffel, ISTerre, Grenoble, France, ⁸Reykjavik Geothermal Ltd., Reykjavik, Iceland

Supporting Information:

Supporting Information may be found in the online version of this article.

Correspondence to:

W. Hutchison,
wh39@st-andrews.ac.uk

Citation:

Hutchison, W., Ogilvie, E. R. D., Birhane, Y. G., Barry, P. H., Fischer, T. P., Ballentine, C. J., et al. (2023). Gas emissions and subsurface architecture of fault-controlled geothermal systems: A case study of the North Abaya geothermal area. *Geochemistry, Geophysics, Geosystems*, 24, e2022GC010822. <https://doi.org/10.1029/2022GC010822>

Received 8 DEC 2022

Accepted 7 MAR 2023

Abstract East Africa hosts significant reserves of untapped geothermal energy. Exploration has focused on geologically young (<1 Ma) silicic calderas, yet there are many sites of geothermal potential where there is no clear link to an active volcano. The origin and architecture of these systems are poorly understood. Here, we combine remote sensing and field observations to investigate a fault-controlled geothermal play located north of Lake Abaya in the Main Ethiopian Rift. Soil gas CO₂ and temperature surveys were used to examine permeable pathways and showed elevated values along a ~110 m high fault, which marks the western edge of the Abaya graben. Ground temperatures are particularly elevated where multiple intersecting faults form a wedged horst structure. This illustrates that both deep penetrating graben bounding faults and near-surface fault intersections control the ascent of hydrothermal fluids and gases. Total CO₂ emissions along the graben fault are ~300 t d⁻¹; a value comparable to the total CO₂ emission from silicic caldera volcanoes. Fumarole gases show δ¹³C of -6.4‰ to -3.8‰ and air-corrected ³He/⁴He values of 3.84–4.11 R_A, indicating a magmatic source originating from an admixture of upper mantle and crustal helium. Although our model of the North Abaya geothermal system requires a deep intrusive heat source, we find no ground deformation evidence for volcanic unrest or recent volcanism along the graben fault. This represents a key advantage over the active silicic calderas that typically host these resources and suggests that fault-controlled geothermal systems offer viable prospects for geothermal exploration.

1. Introduction

The East African Rift System (EARS) hosts a wide range of volcanoes and geothermal resources (Biggs et al., 2021). Although these systems offer huge benefits in terms of clean, renewable energy, few sites have been fully explored, let alone developed (Kombe & Muguthu, 2018). Over the last few decades, new insights into the origin, architecture and stability of East Africa's geothermal resources have come from studies of ground deformation (e.g., Albino & Biggs, 2021; Biggs et al., 2009, 2011; Temtime et al., 2018), magnetotellurics (e.g., Samrock et al., 2015, 2018); seismicity (e.g., Nowacki et al., 2018; Simiyu & Keller, 2000; Wilks et al., 2017), gas emissions (e.g., Hutchison et al., 2015, 2016), and fluid geochemistry (e.g., Pürschel et al., 2013). These studies emphasize that the most promising geothermal resources are associated with volcanic calderas. In these systems, hydrothermal fluids are derived from meteoric sources (Darling et al., 1996; Rango et al., 2010), while heat is supplied by long-lived silicic magma reservoirs (Iddon et al., 2019). High temperature, convecting geothermal fluids are trapped beneath a relatively shallow (0.5–2 km deep) impermeable clay cap layer and tectonic faults play a key role in directing the flow of these fluids toward the surface (Hutchison et al., 2015; Samrock et al., 2018). Although the deep (km-scale) architecture of these volcanic-geothermal systems is best imaged by magnetotellurics, high-spatial resolution (~10–50 m) gas surveys are particularly powerful at identifying permeability and pinpointing drilling locations (Jolie et al., 2019).

Though many of East Africa's geothermal resources fit this model and are intimately associated with silicic caldera complexes, there are various sites which show geothermal manifestations and high fluxes of magmatic

© 2023. The Authors.

This is an open access article under the terms of the [Creative Commons Attribution License](https://creativecommons.org/licenses/by/4.0/), which permits use, distribution and reproduction in any medium, provided the original work is properly cited.

volatiles but no surface volcanism. These areas are associated with tectonic faulting and include the Natron and Magadi basins at the Kenya-Tanzania border (Lee et al., 2016, 2017; Muirhead et al., 2016) and the Habilo area NW of Fantale in the Main Ethiopian Rift (MER) (Hunt et al., 2017). To date, few studies have investigated the architecture and potential of these fault-controlled geothermal systems. However, when compared to the silicic calderas (which pose considerable volcanic eruption hazards that could lead to damage and disruption of geothermal infrastructure, Fontijn et al., 2018; Clarke et al., 2020; Tierz et al., 2020), these fault-controlled geothermal areas are potentially much lower risk and therefore safer options for exploration, investment and development.

Here, we bring together new remote sensing and gas emission data from the North Abaya geothermal area in the MER, which is a fault-controlled geothermal play that shows no surface volcanic edifice. North Abaya is consistently highlighted as one of Ethiopia's key geothermal prospects (Burnside et al., 2021), and although previous studies have investigated regional volcano-tectonic activity (Corti et al., 2013; Ogden et al., 2021) and documented surface geothermal manifestations (i.e., hot springs and fumaroles, Craig et al., 1977; Chernet, 2011; Minissale et al., 2017) there is no conceptual model to understand the heat source, fluid flow, gas emissions and geothermal potential of the resource. We show that a large offset graben bounding fault plays a key role in channeling gas and hydrothermal fluids toward the surface, and while there is no evidence for volcanism along the fault, a deep magmatic heat source is still required. Gas emissions along this fault zone are comparable to sites of proven geothermal resources in Ethiopia (e.g., the silicic caldera of Aluto) and while there are fundamental differences between the North Abaya geothermal play and the silicic calderas, our conceptual model suggests that there is great potential for further exploration and development.

2. Geological Setting

2.1. The Main Ethiopian Rift (MER)

The MER (Figure 1) is the northernmost segment of the EARS and accommodates E-W extension between the Nubia and Somalia Plates (Corti, 2009). The region is extending at 4–6 mm yr⁻¹ (e.g., Saria et al., 2014) and this is accommodated by both faulting and magmatic intrusion (Corti et al., 2013; Ebinger, 2005; Keir et al., 2006). The MER is subdivided into northern (NMER), central (CMER), and southern (SMER) segments and there is a broad consensus that rift maturity decreases southwards (Agostini et al., 2011). One of the most fundamental differences is the style and location of volcano-tectonic activity. In the NMER, border faults, with large vertical offsets > 100 m, define the boundaries of the rift but are largely abandoned (Casey et al., 2006; Keir et al., 2006; Wolfenden et al., 2004). Active seismicity and magmatic intrusion in the NMER is instead focused along the axis of the rift (Ebinger & Casey, 2001; Keir et al., 2006; Kendall et al., 2005) in a region commonly referred to as the Wonji Fault Belt (e.g., Boccaletti et al., 1999; Gibson, 1969; Mohr, 1967). In the SMER, the focus of this study, geological and geophysical data show very different patterns and indicate that border faults still accommodate significant extension (Corti et al., 2013; Kogan et al., 2012; Philippon et al., 2014). Recent volcanism is collocated with border faults along the rift margins (Corti et al., 2013; Rooney et al., 2011), again, contrasting with the focused axial magmatism observed in more northerly segments of the MER.

Bimodal volcanism due to rift-related magmatic intrusion is abundant throughout the MER. Mafic lava flows and scoria cone fields are abundant, as are highly evolved peralkaline rhyolitic complexes (Gibson, 1969; Hutchison et al., 2015; Hunt et al., 2019, 2020). Primitive mantle-derived melts are stored at depths of ~15 km beneath the surface where they form dyke complexes and undergo mafic fractionation (Iddon & Edmonds, 2020). Such dykes are thought to then undergo either rapid transition to the surface where they erupt as monogenetic cinder cones (Mazzarini et al., 2013; Rooney et al., 2011) or are focused toward shallow (~5 km deep) silicic magma bodies where they undergo more extensive crystal fractionation to form trachytic and rhyolitic melts (Iddon et al., 2019; Peccerillo et al., 2003; Rooney, Hart, et al., 2012). These erupt to form a thick pile of coalescing rhyolitic lava flows and domes, pumice cones, and pyroclastic deposits (Hunt et al., 2019; Hutchison et al., 2015, 2016).

2.2. Volcanic and Tectonic Features of the North Abaya Geothermal Area

The North Abaya geothermal area is located in the Soddo area of the SMER (Corti et al., 2013; Figures 1 and 2a). Here, like many areas of the MER, surface geology is typified by NE-SW trending faults and bimodal volcanism (primarily mafic scoria cone fields and larger, 3–15 km wide, silicic centers and calderas). Mapping of regional fault structures by Chernet (2011) and Corti et al. (2013) identified a prominent network of right-stepping

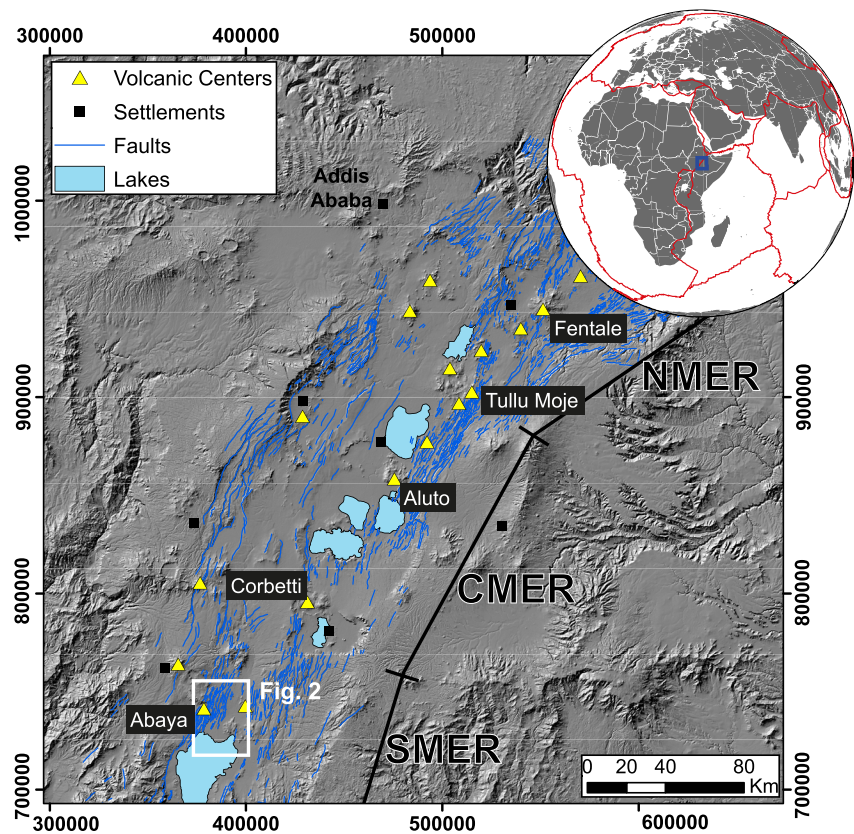


Figure 1. Hillshade Satellite Radar Topography Mission digital elevation model (DEM) of the Main Ethiopian Rift (MER). The MER is divided into northern, central, and southern segments (NMER, CMER, SMER) and fault structures (modified after Agostini et al., 2011) are shown as blue lines. Volcanic centers are shown by yellow triangles, lakes are shaded blue and large settlements are shown by black squares. The Abaya volcanic field is located within the white rectangle. The globe inset shows major plate boundaries in red and the region covered by the DEM as a blue square.

en echelon normal or oblique faults, with vertical offsets generally <100 m, and lengths of 1–10 km. Corti et al. (2018) showed that rift architecture in this sector of the SMER is asymmetric, with the eastern side of the rift characterized by a single large offset border fault (the Agere Selam escarpment), while the western side is characterized by the aforementioned closely spaced, small offset normal faults. Corti et al. (2018) described the western margin in the Soddo area as a rift-ward dipping monocline where a dense concentration of boundary faults results in a staggered uplift toward the rift flank over 10–20 km (Figure 2b; Corti et al., 2013). Across this rift border zone, where our study area is located, three prominent graben structures are observed and from west to east these are the Salewa Dore-Hako graben, the Abaya graben and the Chewkare graben (Figure 2c and Section 4.1). Tectonic activity in this region has occurred through the Late Pleistocene-Holocene (Corti et al., 2013) and there is ongoing seismicity associated with this border fault zone (Ogden et al., 2021).

Recent volcanism is concentrated in the Salewa Dore-Hako Graben and includes isolated mafic scoria cones and the 3.5 km wide, 250 m high Salewa Dore-Hako rhyolite complex (Figure 2a). Both the mafic and silicic vents show alignment with nearby graben faults, indicating important fault controls on magma ascent (noted previously by Corti et al., 2013, and at other Ethiopian rift volcanoes, cf. Hutchison et al., 2015; Hunt et al., 2020). Although robust age constraints on volcanism in North Abaya are currently lacking, the collocation of fumaroles at mafic and silicic vents attests to very recent, most likely Holocene, eruptive activity probably coincident with episodes of faulting (Corti et al., 2013).

Various geothermal features have been identified in the North Abaya area (summarized in Figure 2a). Of these the most vigorous thermal manifestations (hot springs and fumaroles with temperatures up to ~95°C, Chernet, 2011) are found 1–2 km north of Lake Abaya along a major fault that bounds the Abaya graben (herein referred to as West Abaya graben fault (WAGF), Figure 2b). Steam vents have also been observed at the summit of the Salewa

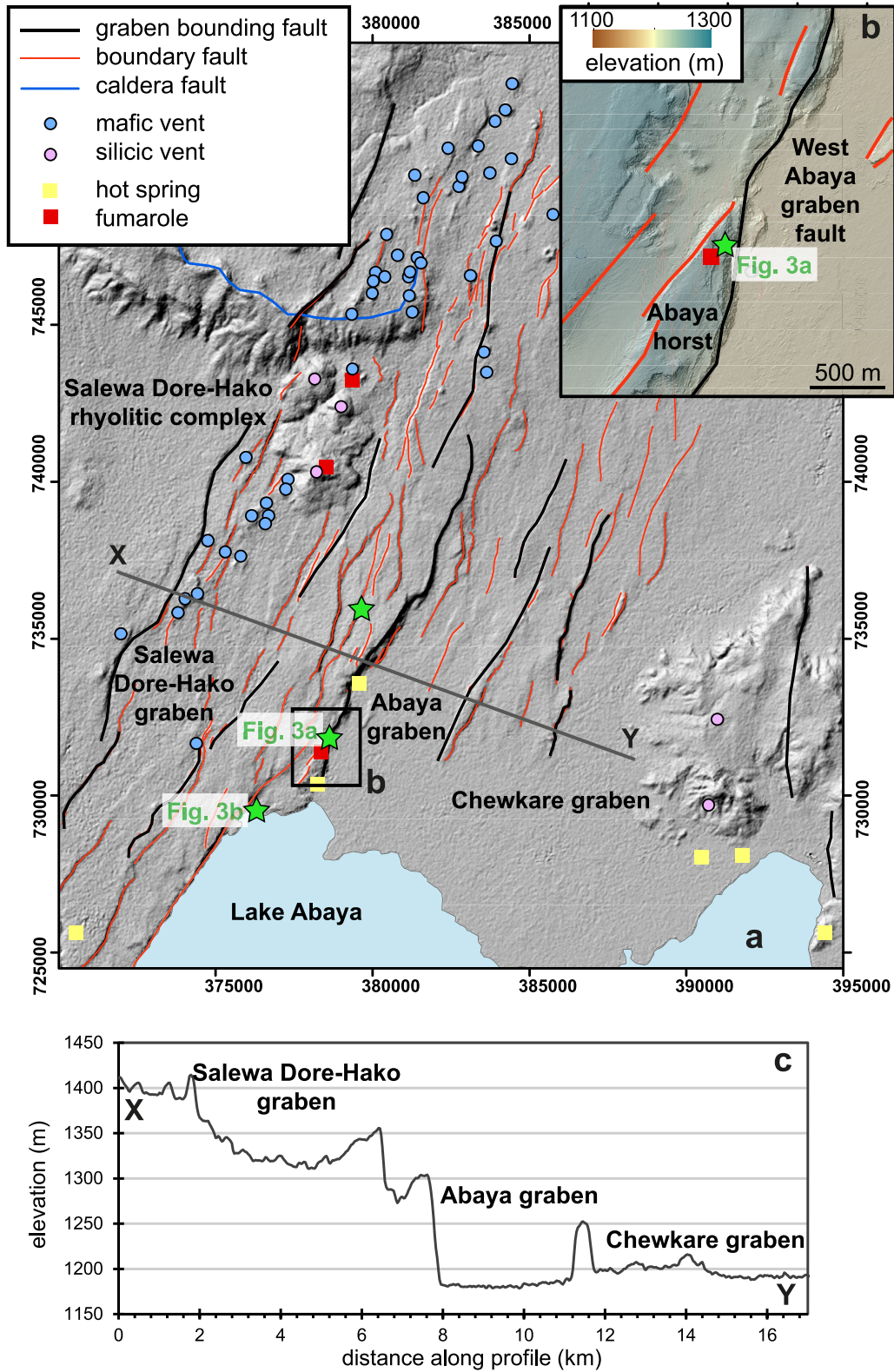


Figure 2.

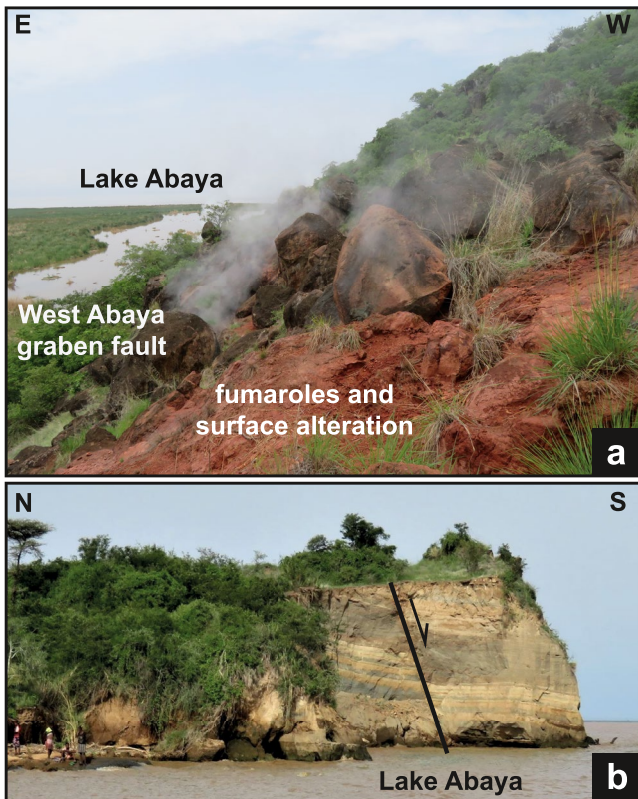


Figure 3. Field photographs. (a) Looking south along the escarpment of the West Abaya graben fault toward Lake Abaya. (b) Looking east toward the southern extent of the Abaya horst. A normal fault dipping toward the south is observed and has a throw of $\sim 2\text{--}3$ m (note people for scale at lower left of image).

Dore-Hako rhyolitic complex (SDHRC) but are of more limited areal extent and intensity with temperatures of $40^{\circ}\text{C}\text{--}90^{\circ}\text{C}$. Geochemical analyses of spring waters in the Abaya region show meteoric isotope compositions with a dominant Na and HCO_3 composition (indicative of water-rock interaction at depth, Minissale et al., 2017). Fumarole gases are notable for their high CO_2 contents (80%–95%) and show He- and C-isotope values that are consistent with mantle sources (Minissale et al., 2017).

In summary, the North Abaya geothermal area (Figure 2) is a zone of recent faulting and volcanism, with the latter mainly confined to the Salewa Dore-Hako Graben. There is evidence for a mature geothermal system (stable over several decades, cf. Chernet, 2011) and the circulating fluids are of meteoric origin, have undergone significant water-rock interaction and are flushed by magmatic gases (Minissale et al., 2017). Despite this, the subsurface architecture of the geothermal system and the relationship between faulting, magmatism and hydrology at Abaya remain poorly understood. Our work addresses this question via remote sensing and high spatial resolution soil gas surveys, which provide important insights into the magmatic-hydrothermal system and allow us to pinpoint the most permeable structures that could be targeted for geothermal drilling (Jolie et al., 2019).

3. Methods

3.1. Remote Sensing

To map volcanic landforms and tectonic structures in North Abaya, we used a 12.5 m digital elevation model (DEM) from the Japanese ALOS satellite (ALOS PALSAR). These data were combined with previous fault data bases of Agostini et al. (2011) and Corti et al. (2013). Ground deformation is frequently observed at geothermal sites in Ethiopia (e.g., Biggs et al., 2011; Birhanu et al., 2018; Hutchison et al., 2016; Lloyd et al., 2018b) and for Abaya, we evaluated this using satellite radar interferometry (InSAR). Recently, Albino and Biggs (2021) used Sentinel-1 data provided by the European Space Agency (ESA) to generate an InSAR time series along the

entire EARS for the period 2015–2020. Here we explore a subset of the data from North Abaya and for full details of the processing, the reader should refer to Albino and Biggs (2021).

3.2. Soil CO_2 Flux and Temperature Surveys

Soil CO_2 flux and temperature were measured in January–February 2019. These months are the driest period in Ethiopia and provide the most stable meteorological and environmental conditions (i.e., there was no significant precipitation nor changes in surface vegetation during our study). The objectives of our survey were first, to transect major rift faults in the SE of the study area and second, to generate detailed maps of soil degassing along the WAGF and the flank of the SDHRC (the main volcanic edifice in the study area, Figure 2a). The typical spatial resolution of our sampling was 50 m and in total 757 measurements were made. CO_2 flux was measured via the accumulation chamber technique (Chioldini et al., 1998; Parkinson, 1981). We used a West systems flux meter with an inbuilt LICOR-LI820 CO_2 concentration sensor and the flux measurement was based on the rate of CO_2 increase in the chamber over a 2-min measurement period. Repeat measurements were typically within 10%–25% and showed better precision in high flux zones. Several low- and high-flux sites were revisited throughout the duration of the campaign, and we found that repeated measurements at the same site were within the above measurement uncertainty. These values are similar to previous geothermal studies (e.g., Hutchison et al., 2015) and are

Figure 2. (a) Hillshade digital elevation model of the North Abaya geothermal area. The main graben bounding faults are shown by the black lines, while other NNE-SSW trending regional faults are shown in red. There are three prominent graben structures in the region: the Salewa Dore-Hako, the Abaya and the Chewkare grabens. Mafic cones and silicic vents are shown by blue and pink circles, respectively. Hot springs and fumaroles are shown by yellow and red squares, respectively. The Salewa Dore-Hako rhyolitic complex is the largest volcanic edifice in the region. Green stars show the location of the photographs in Figure 3. (b) Shaded relief map showing the Abaya horst, which is formed at the intersection of NNE-SSW trending regional faults and the main West Abaya graben fault. (c) Elevation cross-section of the Abaya area. The location of section X-Y is shown in (a).

typical of the instrument reproducibility and natural variations in emission rates (Carapezza & Granieri, 2004; Chiodini et al., 1998; Giammanco et al., 2007; Viveiros et al., 2010).

At each station, we measured soil temperature using a Digi-Sense Type K thermocouple probe and an Oakton Temp 10 Thermocouple Thermometer inserted into 50 cm soil depth. To create the measurement hole, we used a sledgehammer to drive a 50 cm metal bar into the ground before inserting the thermocouple. Note that in all cases CO₂ flux was measured before the 50 cm hole was made and since penetration through the soil causes frictional heat, the probe was left in place until a stable temperature reading was obtained. In some locations the 50 cm depth could not be reached (due to stones or bedrock) and so the depth of the probe was recorded as well as the temperature (Data Set S1).

In areas of volcanic-hydrothermal gas emissions, there are usually multiple sources of CO₂ (i.e., magmatic gases variably mixed with biogenic and terrestrial background). Chiodini et al. (1998) applied a graphical statistical approach (originally by Sinclair, 1974) to demonstrate that volcanically influenced degassing areas often show bimodal CO₂ flux populations, and that these populations can be distinguished using the inflection points on logarithmic probability plots. In our study, we used probability plots and the inflection points to identify different background and volcanic-hydrothermal populations in both our temperature and CO₂ flux data sets (Section 4.3). To produce maps of CO₂ flux and temperature, we used a sequential Gaussian simulation (sGs) method (Cardellini et al., 2003). These methods allow the user to undertake hundreds of realizations of the survey grid and are particularly useful for CO₂ because they constrain the uncertainty in the total flux. sGs methods require a high sampling density and hence were attempted only on the Western flank of the Abaya Graben and the flank of the SDHRC. Three hundred sGs were performed using the sgsim simulation tool (Deutsch & Journel, 1998) in the Stanford Geostatistical Modeling Software (SGeMS) package (Remy et al., 2009). To generate maps, we calculated the arithmetic mean of each individual cell across all simulations and for CO₂, we calculated the total flux of each simulation and used this to compute the mean and standard deviation of all simulations and assess total CO₂ emission and its uncertainty.

3.3. Gas Sampling and Geochemical Analysis

3.3.1. Bulk Gas Chemistry and Carbon Isotopes

Dry gas samples from gas-rich springs and fumaroles were collected in 9 ml preevacuated tubes. These samples were then analyzed for bulk chemistry and C isotopes ($\delta^{13}\text{C}$) at the Department of Earth and Planetary Sciences at the University of New Mexico (UNM). Gas chromatography (GC) and quadrupole mass spectrometry (QMS) were used to measure CH₄-CO₂-H₂-CO and Ar-He-N₂-O₂ concentrations, respectively. The analytical setup used at UNM is identical to that of Lee et al. (2017) and is described in detail therein. Experimental errors for the GC and the QMS are <2 and <1% respectively. Due to the collection of samples in glass vials with rubber septa, He and H₂ are likely to rapidly diffuse out of the vials and results for these gas species are not representative of the composition of the gas discharge.

Samples with the highest concentrations of CO₂ were selected for $\delta^{13}\text{C}$ analysis using a Thermo Scientific Delta Ray Infrared Spectrometer. The samples were diluted using the capillary dilution system provided by the manufacturer and introduced into the inlet of the instrument through a needle and capillary. In order to compensate for pressure decrease during analyses, a pure N₂ gas was connected to the vial. Calibration was performed prior to and following the analyses with a commercially available calibration gas and all CO₂- $\delta^{13}\text{C}$ measurements are shown in delta notation as per mil values ($\delta\text{‰}$) relative to Vienna Pee Dee belemnite (VPDB). Our measurements are characterized by a $\delta^{13}\text{C}$ standard error of $\pm 0.1\text{‰}$.

3.3.2. Helium Isotopes

For helium isotope measurements gases were collected in Cu-tubes from moderate to high temperature (60°C–95°C) bubbling springs and fumaroles. At each locality, samples were collected using (3/8-inch) Cu-tubes connected at one end with Tygon tubing fitted with an inverted funnel, which was inserted into the source of gas manifestation (e.g., Kennedy et al., 1985; Weiss, 1968). The other end of copper tube was fitted with a second section of Tygon tubing, a second copper tube and a third section of Tygon tubing, which was submerged in water to ensure a one-way flow of gas through the sampling apparatus, thus minimizing air contamination. Approximately 1–2 hr were taken to flush the entire sampling apparatus before sealing both ends of the copper tubes using specially designed stainless-steel clamps that create a cold-weld in the Cu-tubing, thus sealing sample gas inside the tube for transport to the laboratory.

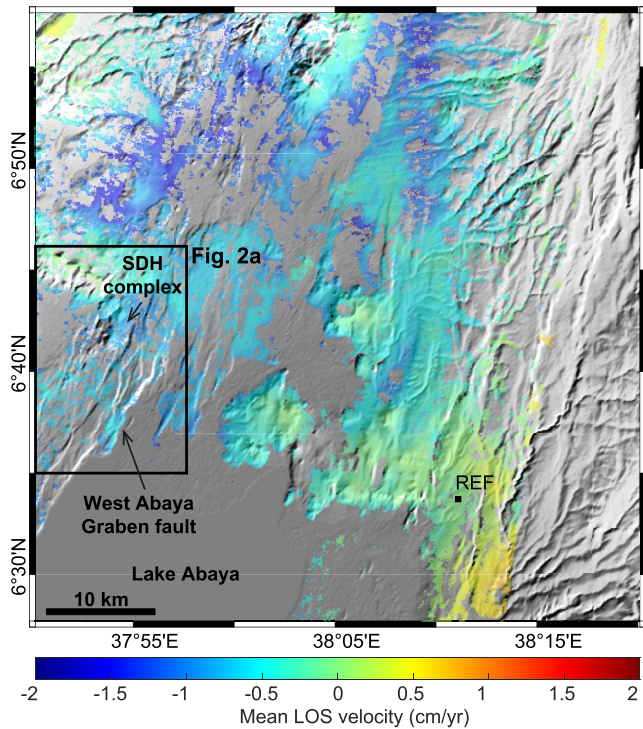


Figure 4. Ground deformation north of Lake Abaya during the period 2015–2020. The results are shown as mean line of sight velocity in cm/yr, relative to a representative reference area (labeled REF) that is well distanced from any volcanic and/or tectonic features (and assumed not to be deforming). Note that SDH indicates the Salewa Dore-Hako rhyolitic complex. Volcanic ground deformation usually results in uplift-subsidence of at least ± 2 cm/yr. In this case, no such deformation signals are detected.

Noble gas isotope analysis was conducted using a dual mass spectrometer setup, interfaced to a dedicated extraction and purification system at the University of Oxford (Barry et al., 2016). In brief, gases collected in Cu-tubes were transferred to the extraction and purification line where reactive gases were removed by exposing gases to a titanium sponge held at 950°C. The titanium sponge was cooled for 15 min to room temperature before gases were expanded to a dual hot (SAES GP-50) and cold (SAES NP-10) getter system, held at 250°C and room temperature, respectively. A small aliquot of gases was segregated for preliminary analysis on a quadrupole mass spectrometer. He and Ne isotopes were then concentrated using a series of cryogenic traps; heavy noble gases (Ar-Kr-Xe) were frozen down at 15 K on a stainless-steel finger and the He and Ne were frozen down at 19 K on a cold finger filled with charcoal. The temperature on the charcoal finger was then raised to 34 K to release only He, which was inlet into a Helix SFT mass spectrometer. Following He analysis, the temperature on the charcoal cryogenic trap was raised to 90 K to release Ne, which was inlet into an ARGUS VI mass spectrometer. Uncertainties on helium isotopes and He/Ne values are less than 3%.

4. Results

4.1. Tectonics and Recent Volcanism

Fault structures in the North Abaya study area are shown in Figure 2. We mapped three major graben structures (the Salewa Dore-Hako graben, the Abaya graben and Chewkare graben) as well as regional faults that define an overall NNE-SSW trend. Graben bounding faults show the greatest displacement (Figure 2c) with the WAGF marked by the largest vertical offset of ~ 110 m. Overall, the North Abaya faults display a right-stepping *en echelon* pattern (Corti et al., 2013), which leads to various intersecting fault zones. This is particularly well developed at the southern end of the WAGF where a ~ 100 m high wedge-shaped horst block is observed (Figure 2b). We refer to this area as the Abaya horst and a field photograph from the west of this structure

looking south shows that this is a site of fumarolic activity where hydrothermal upwelling has led to surface alteration and the formation of bright red clays. On the ground, these fumaroles display a WNW-ESE alignment, which suggests that these vents are linked to WNW-ESE structures orthogonal to the WAGF. Importantly, we found field evidence for the existence of such faults along the shore of Lake Abaya, where a WNW-ESE fault with a throw of 2–3 m was observed (Figure 3b). We suggest that although major NNE-SSW rift-aligned tectonic faults accommodate the bulk of extension, their *en echelon* fabric creates numerous intersecting fault sets that may develop into highly fractured “gridded” fault zones (as seen in the Abaya horst).

Our mapping of volcanic vents shows that these are mainly located in the Salewa Dore-Hako graben (in agreement with previous studies, Corti et al., 2013). Mafic scoria cones define a ~ 20 km long NNE-SSW trend, while silicic vents are focused at the ~ 5 km long \sim N-S oriented SDHRC which comprises overlapping obsidian coulees. The overall NNE-SSW alignment of the mafic vents suggests a feeder dyke of similar orientation (Corti et al., 2013), while the more chemically evolved silicic volcanism is indicative of an upper crustal (~ 5 km deep) magma reservoir as observed elsewhere in the rift (e.g., Aluto, Hutchison et al., 2016; Gleeson et al., 2017; Iddon et al., 2019). Fumaroles are observed at the SDHRC, but are much weaker than those observed along the WAGF (Figure 3a).

4.2. Ground Deformation

The results of a 2015–2020 Sentinel-1 InSAR survey for the North Abaya region are shown in Figure 4. The map shows the mean line of sight velocity (in cm yr^{-1}) relative to a reference area that is located >30 km east of the study area and well distanced from any volcanic or tectonic features. Deformation rates in the North Abaya geothermal area are on the order of 0 to -0.5 cm yr^{-1} . Albino et al. (2022) investigated limits of detection in this Sentinel-1 time series and demonstrated that linear deformation rates must be greater than 0.5 cm yr^{-1} to be detected over this 5-year period. At North Abaya, deformation rates (Figure 4) clearly fall

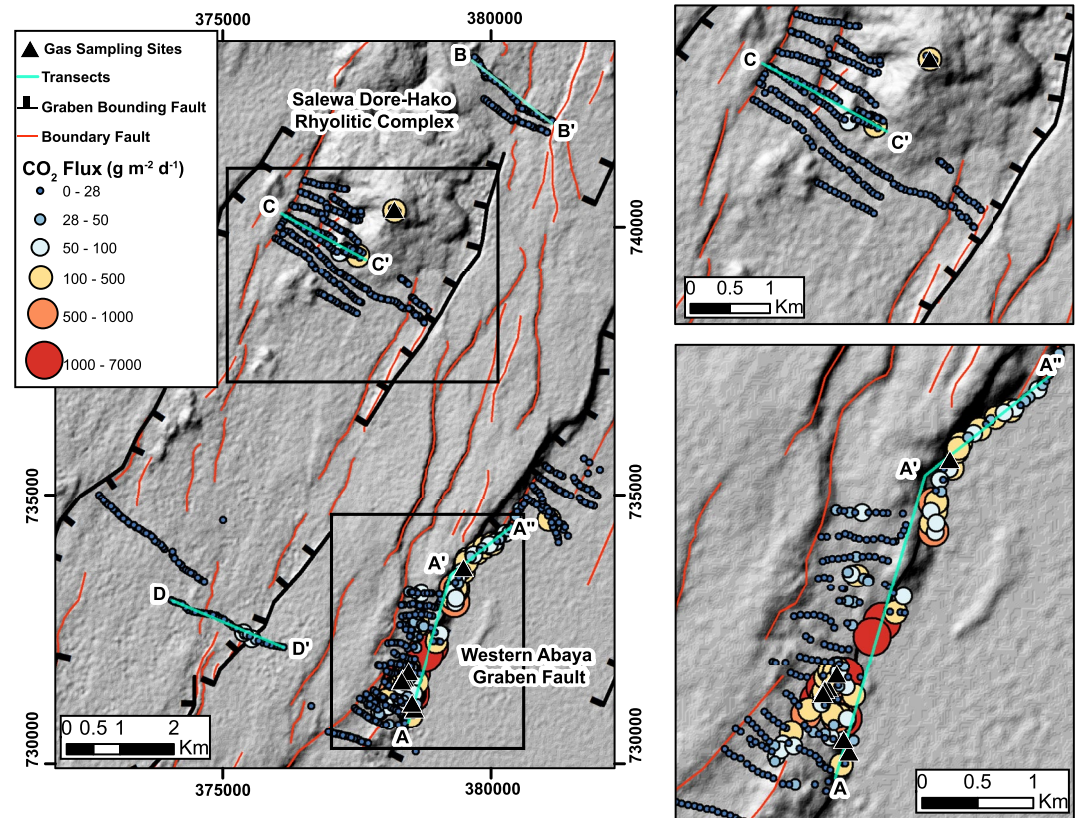


Figure 5. Hillshade digital elevation model overlain with soil CO₂ flux values. The magnitude of the soil CO₂ flux corresponds to the size of the circle in accordance with the key on the left of the plot. Note that the smallest circles are typical of the background, whereas larger circles are indicative of a volcanic-hydrothermal origin. Insets show CO₂ degassing at the Salewa Dore-Hako Rhyolitic Complex and West Abaya graben fault (in the upper and lower right-hand panels, respectively). Transects of the CO₂ degassing data set are shown by the turquoise lines and are labeled as A-A', B-B', and C-C'.

below the limits of detection and are negligible when compared to uplift/subsidence signals that typify other East African volcanoes that host geothermal resources (typically >2 cm yr⁻¹, Albino & Biggs, 2021). Thus, our data show that there was no significant deformation in the North Abaya study area during the 2015–2020 period.

4.3. CO₂ Degassing and Soil Temperatures

Maps of CO₂ flux and soil temperatures are shown in Figures 5 and 6, respectively. CO₂ flux ranged from 0.2 to 6,020 g m⁻² d⁻¹ and showed elevated values along the WAGF, with the highest values observed around the northern wedge of the Abaya horst. A few elevated CO₂ flux values were observed at the SDHRC and along graben bounding faults, but within the center of the grabens, fluxes were low (Figure 5). Soil temperatures (Figure 6) were between 18.3°C and 98.5°C. They also show high values associated with the WAGF, but unlike CO₂, elevated temperatures were only observed at the northern wedge of the Abaya horst rather than along the length of the fault. Temperatures were low (<45°C) on the SDHRC except for some weak fumaroles located on the top of the complex.

To evaluate the existence of different CO₂ and temperature sources, we examined probability plots (Figure 7). It is expected that when data consist of a single log-normal population, this will plot as a straight line, and when there are multiple log-normal populations, these will plot as curves of overlapping populations defined by inflection points (Chiodini et al., 1998). Our CO₂ flux and soil temperature data show clear inflection points at values of 28.2 g m⁻² d⁻¹ and 40°C, respectively. We interpret these two populations as (a) a magmatic-hydrothermal source (associated with high temperatures and high CO₂ flux) and (b) a background source (associated with low temperatures and low CO₂ flux, and most likely derived from biogenic and/or deep magmatic/mantle sources). In Figures 8 and 9 we show transects along and across the major faults and volcanic areas of the study area, and

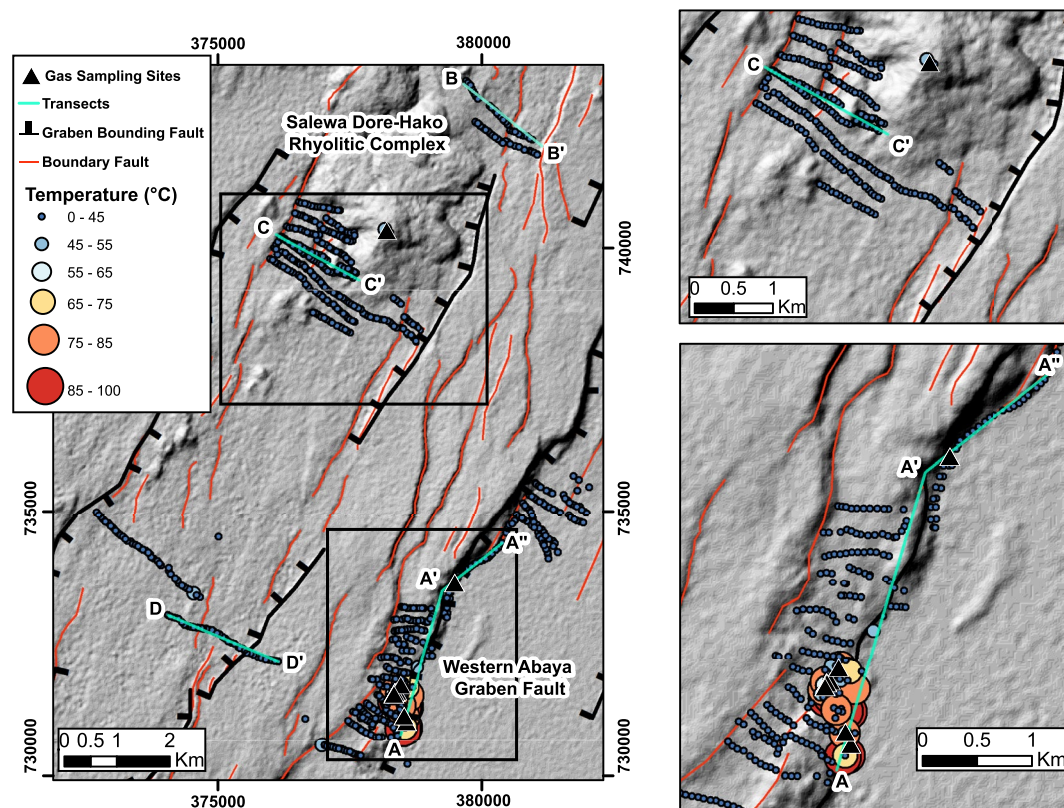


Figure 6. Hillshade digital elevation model overlain with soil temperature values. The magnitude of the soil temperature corresponds to the size of the circle in accordance with the key on the left of the plot. Note that the smallest circles are typical of the background, whereas larger circles are indicative of upwelling hydrothermal. Insets show soil temperatures at the Salewa Dore-Hako Rhyolitic Complex and West Abaya graben fault (in the upper and lower right-hand panels, respectively). Transects of the data set are shown by the turquoise lines and are labeled as A-A'-A'', B-B', and C-C'.

we use the upper value of the background population to help identify areas of significant magmatic-hydrothermal input.

Before looking at transects in detail, it is important to point out two notable features of the background population. First, while background CO_2 flux at North Abaya ($0.2\text{--}28.2 \text{ g m}^{-2} \text{ d}^{-1}$) is within the range of typical nonvolcanically influenced soil ($10\text{--}30 \text{ g m}^{-2} \text{ d}^{-1}$, Mielnick & Dugas, 2000; Rey et al., 2002; Cardellini et al., 2003) it is higher and more variable than other sites in the MER (i.e., $0.5\text{--}6.0 \text{ g m}^{-2} \text{ d}^{-1}$ at $10\text{--}20 \text{ km}$ distance from Aluto volcano, Hutchison et al., 2015). Second, within the background CO_2 flux population, we noted minor inflections at 12.6 and $2.0 \text{ g m}^{-2} \text{ d}^{-1}$ (Figure 7a). The first feature is explained by the fact that North Abaya is much more vegetated than the area surrounding Aluto (the former is adjacent to a large lake and within a major river catchment) and therefore the soil is richer in organic material and hence biogenic CO_2 flux is almost certainly higher. The second feature, regarding multiple minor inflections in the log-probability plot, suggests that there may be several background CO_2 flux populations. Interestingly, some of the more elevated background values do appear to be associated with rift aligned faults (e.g., the red labeled fault in Figure 9, C-C' shows a CO_2 flux $26 \text{ g m}^{-2} \text{ d}^{-1}$). An explanation is that these faults have enhanced permeability and a greater deep magmatic/mantle CO_2 flux that is unrelated to any near surface volcanic-hydrothermal system. We did not collect C isotope samples for these different background sites; therefore, we cannot be certain whether there is a stronger biogenic fingerprint at Abaya, and whether elevated background values associated with faults display a magmatic signature. For completeness, we include these inflection points in the background population in Figures 8 and 9, and we emphasize that while the high temperature, high CO_2 flux magmatic-hydrothermal source is clearly defined, there is undoubtedly a range of biogenic and deep mantle/magmatic CO_2 sources captured in the background population.

Given this broad categorization of magmatic-hydrothermal and background populations, we can take a more detailed look at spatial variations in soil CO_2 flux and temperature using transects (shown in map view in Figures 5

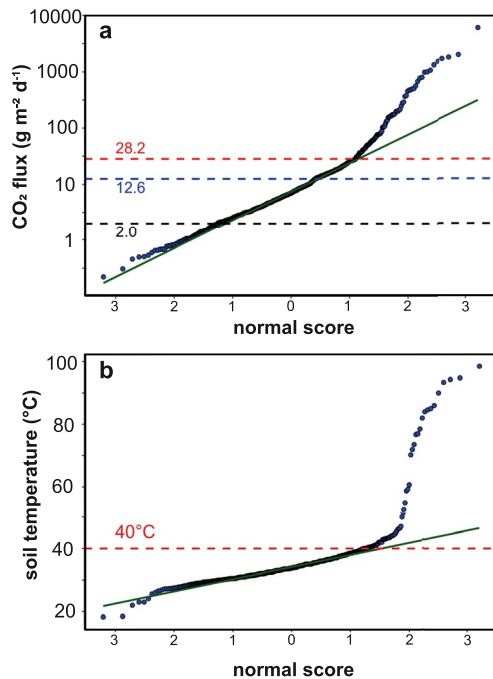


Figure 7. Probability plot of (a) soil CO₂ flux and (b) soil temperature. Inflection points in the probability plot are used to identify different background and volcanic-hydrothermal populations (see Chiodini et al., 1998). For temperature, there is an obvious inflection at 40°C, which is the upper limit of the background values. For CO₂ the main inflection point is observed at 28.2 g m⁻² d⁻¹ and separates background from volcanic-hydrothermal populations. Minor inflections are observed in the background population, and we speculate that these could represent differences between faulted and nonfaulted areas in regions where there is no underlying hydrothermal system (see Section 4.3 for discussion).

and 6, and as plots in Figures 8 and 9). Transect A-A'-A'' shows CO₂ flux and temperature from south to north along the WAGF (Figure 8). CO₂ flux is variable along the fault but shows highest values at the Abaya horst and a maximum value of 6,020 g m⁻² d⁻¹ in the area ~500 m north of this structure. Maximum CO₂ flux values then show a general northward decrease to more typical background values. It is important to note that between ~1,500 and ~2,300 m along the profile we were unable to access the hanging wall of the fault because of surface water, and so the lack of high CO₂ in this area likely reflects a gap in sampling rather than a genuine decrease in CO₂ flux in this section of the fault. Soil temperature also shows highest values at the Abaya horst (up to 98.5°C at the fumaroles in Figure 3a). Notably, between 2,300 and 3,500 m there is elevated CO₂ but only a few temperatures >40°C (Figure 8). This demonstrates that CO₂ flux and soil temperature are not always correlated and therefore CO₂ and hydrothermal steam do not always travel together.

Transect B-B' includes several fault structures in the Salewa Dore-Hako graben and then rises eastward on the flank of the SDHRC (Figure 9). No significant temperature anomalies were detected along this profile. CO₂ flux showed no evidence for elevated values across the intragaben faults but did show several elevated values up to 176 g m⁻² d⁻¹ on the volcanic complex. These maximum CO₂ values are an order of magnitude lower than those obtained on the WAGF (Figure 8). The elevated CO₂ flux on the volcanic complex appears to be localized (Figure 5) and does not show an obvious NNE-SSW (fault controlled) trend, arguing against a tectonic control on CO₂ degassing. Instead, there appears to be a closer relationship between CO₂ flux and elevation, with peak values in CO₂ approximately centered on a topographic high.

Transect C-C' covers the eastern escarpment of the Salewa Dore-Hako graben as well as a regional fault to the west of this (Figure 5). Although the vertical offset for these faults are broadly comparable (~20 and ~15 m for the graben fault and regional fault, respectively) there is a marked contrast in their CO₂ emission with the regional fault showing subtle variation in background

values and the graben fault showing a ~400 m wide zone of elevated values (up to 58 g m⁻² d⁻¹). This finding suggests that the graben bounding faults provide more permeable conduits for deeper magmatic-hydrothermal gases.

Our high-density survey grid along the WAGF and the flank of the SDHRC allowed us to construct maps of CO₂ flux and temperature using sGs methods (Figure 10). Omnidirectional variograms of normal scores were computed for each area and the modeled variogram and parameters are shown beside each map. The results mirror the trends in the underlying data (i.e., Figures 5 and 6) and clearly indicate highest CO₂ flux and temperatures along the WAGF, particularly at the wedge of the Abaya graben. For CO₂ we calculated the total flux (shown as mean ± standard deviation) and the key finding is that while the two survey sites cover a similar area (3.8 and 3.9 km²), the total flux along the WAGF is 294 ± 71 t d⁻¹ which is 10× greater than that on the flank rhyolitic complex (29 ± 3 t d⁻¹).

4.4. Gas Chemistry

Compositions of gas samples are shown in Table 1. Our samples mainly contain N₂, O₂ and CO₂ and represent air that has been flushed by gases of magmatic-hydrothermal origin. Those samples that are rich in CO₂ (up to 30%–36%) represent the most pristine magmatic gas samples. Minor gas species include He, H₂, Ar, CH₄, and CO, which originate from a combination of atmospheric and magmatic sources, as well as reducing reactions in the hydrothermal reservoir (i.e., CH₄ and CO, Agosto et al., 2013; Tassi et al., 2013).

New carbon isotope (δ¹³C) data for CO₂ from Abaya are compared to previous measurements from volcanic-hydrothermal systems across the East African Rift in Figure 11a. Our Abaya data show values from -6.4‰ to -3.8‰ which are almost identical to previous δ¹³C-CO₂ made at the same localities by Minissale

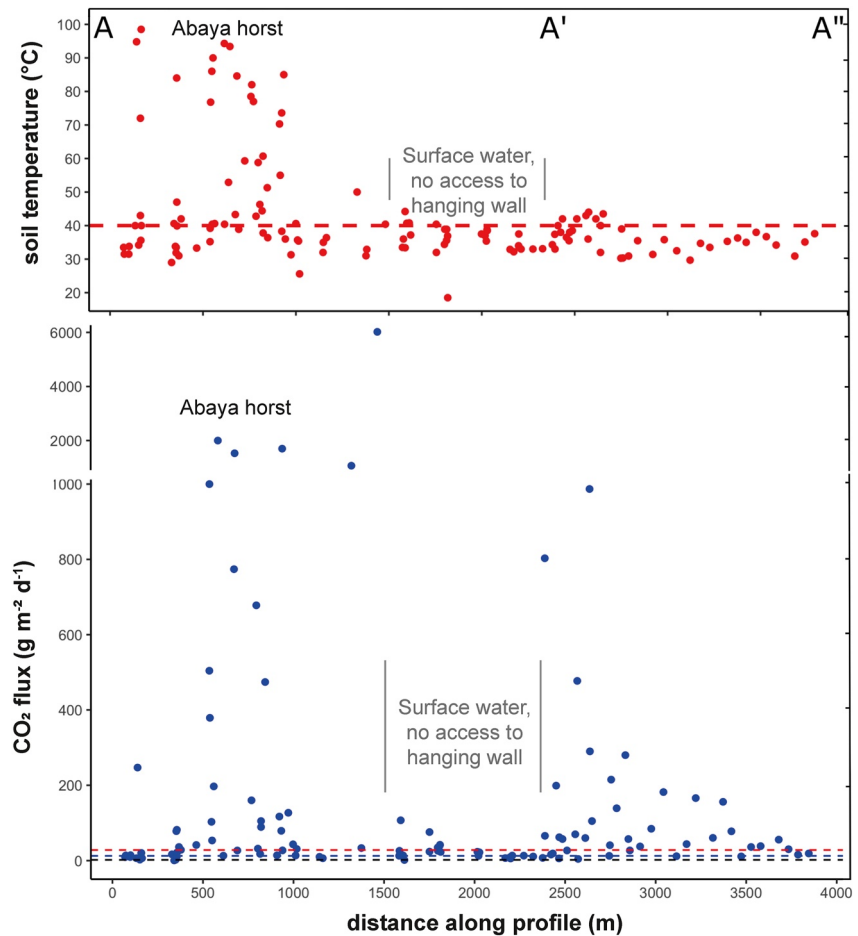


Figure 8. Soil temperature and CO₂ flux along the Western Abaya graben fault, A-A'-A'' (in Figure 5). Red horizontal lines denote the maximum value for background soil temperatures and CO₂ degassing, while the blue and black dashed lines represent minor inflections in background CO₂ populations referred to in Section 4.3. CO₂ flux and temperature are greatest around the wedge of the Abaya horst (i.e., toward the southern extent of the Western Abaya graben fault). Note that between ~1,500 and ~2,300 m along the profile, we were unable to access the hanging wall of the fault because of surface water. The lack of high CO₂ in this area likely reflects a gap in sampling rather than a genuine decrease in CO₂ flux in this section of the fault. The data that are shown in this area are from the footwall.

et al. (2017). Plotting the isotope data versus the reciprocal of CO₂ concentration in the samples reveal a crude triangular array that is usually interpreted as mixing between air, biogenic and magmatic CO₂ (Figure 11a, where end-member δ¹³C values come from Gerlach & Taylor, 1990; Javoy & Pineau, 1991; Macpherson & Matthey, 1994; Sano & Marty, 1995; Darling et al., 1995; Cheng, 1996; Chiodini et al., 2008 and Tedesco et al., 2010). The Abaya gas samples were all extracted from fumarole vents and are clearly focused on the magmatic endmember. This contrasts with previous surveys of the Magadi-Natron rift basin (Lee et al., 2016; Muirhead et al., 2020) and the Aluto geothermal system (Hutchison et al., 2016), which sampled soil gas at both fumarolic and nonfumarolic sites and therefore showed a wider spread of both δ¹³C and CO₂ concentration. Focusing on the magmatic endmember (Figure 11b) reveals that in the most pristine magmatic gas samples, there is overlap between Abaya and Aluto (currently Ethiopia's only developed geothermal site).

Helium isotopes are shown in Figure 11c. The X-value gives the ⁴He/²⁰Ne ratio of the sample relative to that measured in air and therefore gives an indication of how much air has been entrained into the sample. X-values close to 1 are air-dominated, and for our samples X-values are 6.3 and 12.8 implying limited air incorporation. Using the X-values we correct our samples for the presence of atmospheric He isotope values (after Hilton, 1996) and this yields He isotope values (R_C/R_A) of 4.4 (Table 1). Again, these values are similar to previous measurements of North Abaya by Minissale et al. (2017), who found R_C/R_A values of 4.5–7.5 at similar locations along the WAGF. Our helium isotopic compositions are lower than MORB-like values (typically 8 ± 1 Graham, 2002) and

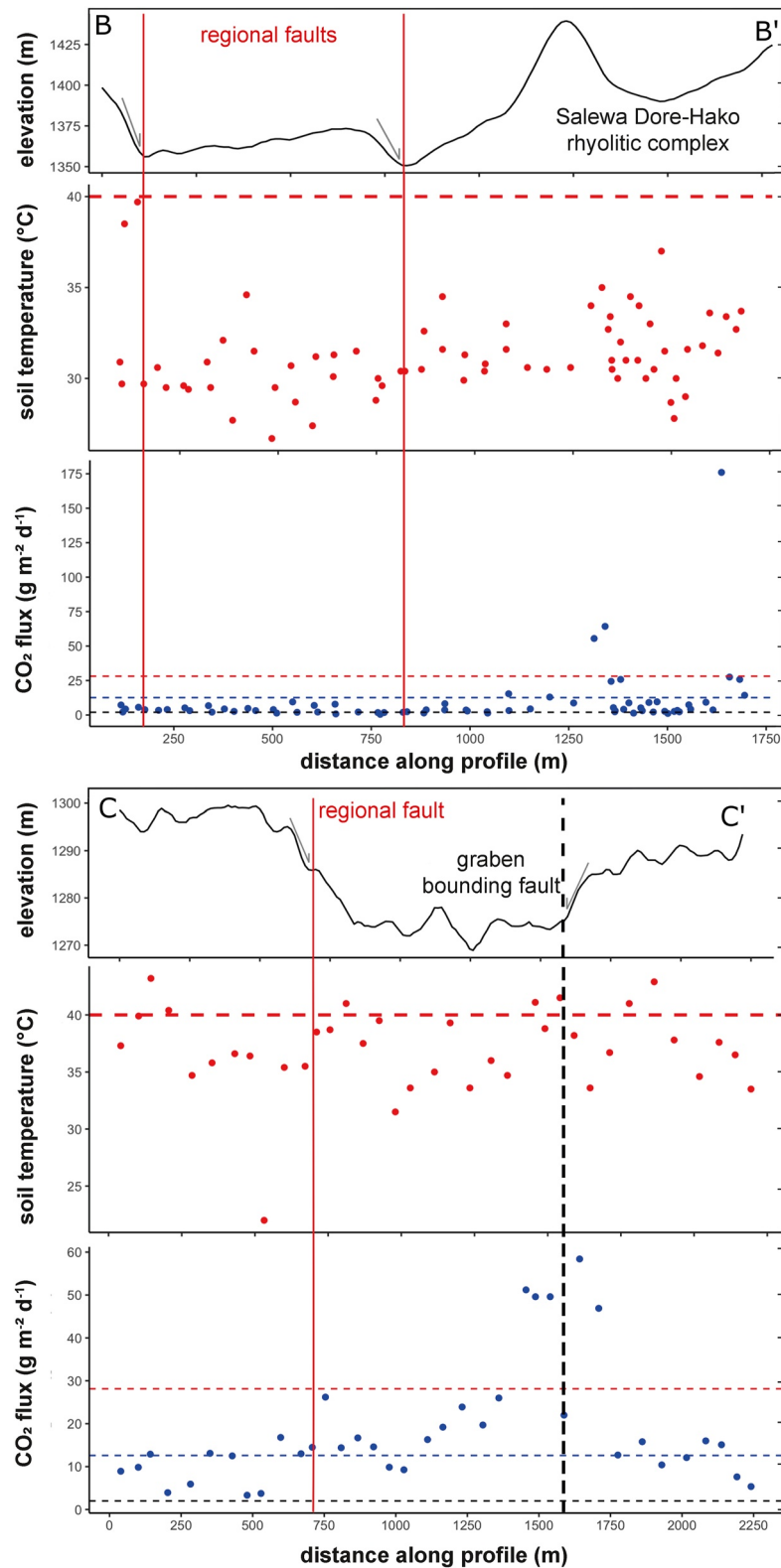


Figure 9. Transects of elevation, soil temperature and CO₂ flux across faults surrounding the Salewa Dore-Hako rhyolitic complex (B-B') and the eastern boundary of the Salewa Dore-Hako graben (C-C'). The vertical, black-dashed line represents the graben boundary fault, while the red lines indicate mapped regional faults. Red horizontal lines denote the maximum value for background soil temperatures and CO₂ degassing, while the blue and black dashed lines represent minor inflections in background CO₂ populations referred to in Section 4.3.

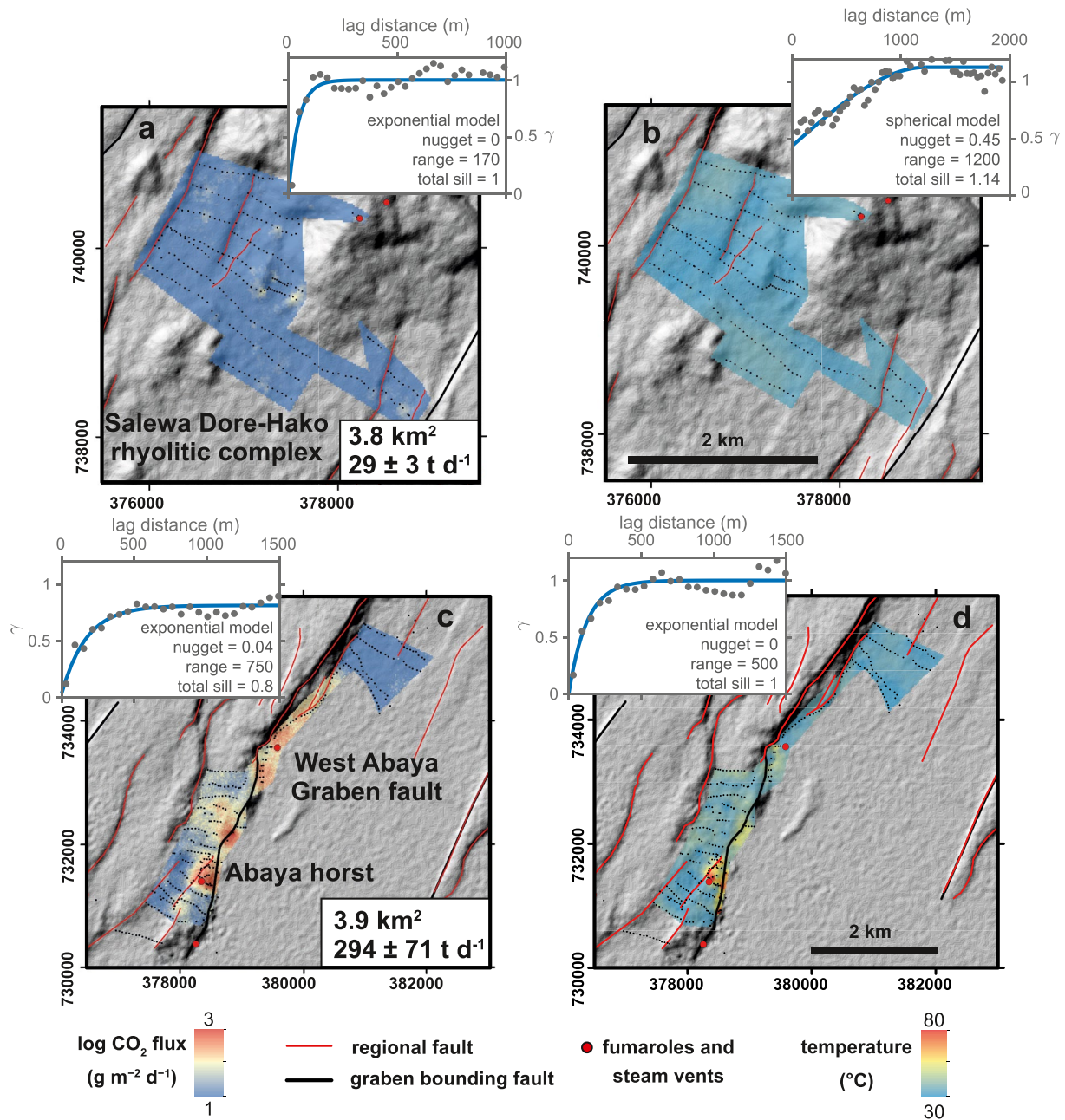


Figure 10. CO₂ flux and temperature maps derived using the sequential Gaussian simulation (sGs) approach for the Salewa Dore-Hako rhyolitic complex (a, b) and the West Abaya graben fault (c, d). Black points represent a discrete flux measurement. Omnidirectional experimental variograms (γ) are shown for each data set. The modeled variogram is shown by the blue line with the key parameters listed.

show close resemblance to a subcontinental lithospheric mantle (SCLM) source (Bräuer et al., 2016; Gautheron & Moreira, 2002; Gilfillan & Ballentine, 2018; Figure 11c).

5. Discussion

5.1. Controls on Volcanism, Hydrothermal Fluids and Degassing

The North Abaya region is dominated by NNE-SSW trending *en echelon* normal faults (Corti et al., 2013), which have an overall horst-graben structure (Figure 2). The Abaya and Chewkare grabens comprise the rift floor, while the Salewa Dore-Hako graben accommodates a transition from the rift shoulder toward the rift floor. The

Table 1
Composition of Samples From North Abaya Geothermal Area

Sample ID	Location	Temperature (°C)	Easting (m)	Northing (m)	CO ₂	He	H ₂	Ar	O ₂	N ₂	CH ₄	CO	δ ¹³ C (‰)	R/R _A	X-value	R _C /R _A
AB-19-G01	SDHRC	50	378192	740329	1.2	0.00	1.0	0.7	17.6	79.3	0.0	0.2	-5.5			
AB-19-G03	WAGF (Abaya horst east)	97	378572	731024	31.7	0.00	0.0	1.1	21.6	44.6	0.5	0.4				
AB-19-G04	WAGF (Abaya horst east)	97	378572	731024	30.7	0.00	0.0	1.2	21.7	45.5	0.5	0.4				
AB-19-G08	WAGF (Abaya horst east)	94.5	378524	731134	0.4	0.00	0.0	1.1	31.4	66.3	0.1	0.6				
AB-19-PB-02	WAGF (Abaya horst east)	94.5	378524	731134	35.5	0.00	0.0	1.1	21.1	41.4	0.5	0.4		3.8	6	4.4
AB-18-G01	WAGF (Abaya horst west)	94	378353	731590	32.0	0.01	2.0	0.6	20.4	44.1	0.5	0.5				
AB-18-G02	WAGF (Abaya horst west)	94	378353	731590	33.2	0.15	3.4	0.6	19.2	42.4	0.5	0.4	-5.0			
AB-18-G03	WAGF (Abaya horst west)	94	378353	731590	33.4	0.01	1.9	0.6	19.4	43.8	0.5	0.4	-3.8			
AB-19-G02	WAGF (Abaya horst west)	97	378387	731603	5.3	0.00	0.0	1.1	20.7	72.7	0.1	0.2				
AB-19-G05	WAGF (Abaya horst west)	95	378337	731548	35.9	0.01	1.8	0.6	18.3	42.5	0.5	0.4	-4.2			
AB-19-G06	WAGF (Abaya horst west)	100	378354	731586	18.0	0.00	2.0	0.6	17.4	61.5	0.2	0.2				
AB-19-G07	WAGF (Abaya horst west)	94	378462	731729	36.3	0.00	1.7	0.6	19.1	40.9	0.6	0.8	-4.3			
AB-19-PB-03	WAGF (Abaya horst west)	93.5	378337	731548	35.7	0.00	0.0	1.1	19.6	43.1	0.1	0.4		4.1	13	4.4
AB-18-G04	WAGF (north of Abaya horst)	58	379479	733655	0.5	0.00	0.4	0.8	21.9	75.6	0.3	0.5	-6.4			
AB-18-G05	WAGF (north of Abaya horst)	58	379479	733655	28.1	0.00	2.7	0.6	14.7	53.8	0.1	0.1	-6.3			

Note. Samples were mainly collected from the West Abaya graben fault (WAGF). Although one sample is from the Salewa Dore-Hako rhyolitic complex (SDHRC). Gas concentrations are reported in mol%. Bulk gas chemistry and C isotopes were measured on samples collected in evacuated glass vials. He isotopes were measured on samples collected in Cu tubes. R/R_A is the measured $^3\text{He}/^4\text{He}$ divided by the $^3\text{He}/^4\text{He}$ in air. X -value is the $^4\text{He}/^{20}\text{Ne}$ ratio of the sample relative to that measured in air. R_C/R_A is the air corrected $^3\text{He}/^4\text{He}$ for the samples using the X -values (cf. Hilton, 1996).

most significant deformation is accommodated on the graben bounding faults and in particular the WAGF which accommodates ~110 m of vertical offset and represents the major structure in the study area. The region either side of a fault plane is referred to as the damage zone and is usually represented by highly fractured and permeable lithologies (Bense et al., 2013). Importantly, fault damage zone width increases with fault displacement (Choi et al., 2016; Faulkner et al., 2011; Knott et al., 1996; Sperrevik et al., 2002). Given that the WAGF shows the greatest displacement, it is also expected to represent the most permeable zone, and this can explain why gas and fluid upflow is concentrated here (as evidenced by fumarolic activity, hot springs and the elevated ground temperatures and CO₂ flux, Figures 3a, 5, and 6). Although the displacement and geothermal activity on the WAGF exceed all other faults, we note that other graben bounding faults do show elevated CO₂ flux (see transect C-C' in Figure 9). While CO₂ flux is much lower, it does suggest that the graben bounding faults are key pathways for CO₂ release and that they are more permeable and/or deeper penetrating than the regional intragaben faults.

Volcanism in the study area is mainly restricted to the Salewa Dore-Hako graben (Figure 2a). Mafic scoria cones span a ~20 km long NNE-SSW oriented trend, while silicic vents are restricted to the Salewa Dore-Hako rhyolitic edifice in the center of this segment. The elongate trend suggests feeder dyke(s) beneath the basin, in agreement with vent elongation (Corti et al., 2013). From our CO₂ flux observations, we identified that graben bounding faults act as high permeability zones. However, volcanic vents are not aligned to these faults and are instead found scattered across the center of the graben. Thus, graben bounding faults do not appear to represent preferential structures for magma ascent and our data suggest that dykes are emplaced in the center of the Salewa Dore-Hako graben and that regional intragaben faults direct magma toward the surface (cf. Corti et al., 2013).

As noted above, the WAGF shows intense surface alteration (Figure 3a) and the most elevated ground temperatures and CO₂ flux in the study area (Figures 5 and 6). High resolution topography (Figure 2b) shows that this margin of the graben is typified by multiple faults which interact and intersect and that the highest ground temperatures are focused in a wedge-shaped zone at the tip of the Abaya horst. Intersecting faults are known to enhance permeability and fluid circulation (Curewitz & Karson, 1997; Person et al., 2012) and we suggest that these interactions at the Abaya horst, as well as the large damage zone of the WAGF, explain why this is an area of intense hydrothermal upflow.

A further feature of the Abaya horst is the occurrence of ~W-E oriented faults (Figure 3a). Although these features have minor offsets (2–3 m) compared to the NNE-SSW aligned faults (10–100 m), it is likely that they also enhance the permeability and direct fluid flow because fumaroles at the tip of the Abaya horst show a WNW-ESE alignment (orthogonal to the trend of the WAGF). Cross rift (~W-E) oriented structures have been documented at many volcanic systems throughout the EARS (Acocella et al., 2003; Benvenuti et al., 2023; Hunt et al., 2019; Lloyd et al., 2018a; E. Robertson, Biggs, Edmonds, et al., 2016), and while we cannot ascertain the extent of these structures at Abaya, they do appear to play an important role directing fluids and gas toward the near surface. In summary, our study reveals that the WAGF controls the main upflow of hydrothermal fluids and gas from depth, and that intersecting faults enhance the permeability of this zone concentrating fluids around the wedge tip of the Abaya horst.

At the Abaya horst, we see high values of both CO₂ flux (2,000 g m⁻² d⁻¹) and ground temperature (>90°C), but it should be noted that this is not the case along the entire length of the WAGF. For example, around A' in our transect in Figure 8 CO₂ is significantly elevated while temperatures are only just above background values of 40°C. This indicates that CO₂ and steam transport are decoupled, and is explained by the fact that steam, which usually travels together with CO₂, has condensed to water during transport. There are several springs and surface water bodies in the vicinity of A', adjacent to the WAGF. Our hypothesis is that steam ascending along this section of the fault intersects groundwater and condenses (i.e., when its temperature drops below 100°C, Fridriksson et al., 2006). CO₂ condenses at much lower temperatures (–78.5°C) and is therefore unaffected by groundwater interactions.

CO₂ flux is also elevated above background values at a few localities on the Salewa Dore-Hako rhyolitic center and the highest values were associated with steaming ground (with temperatures of 50°C). Our study mainly covered the SW flank of the rhyolitic center and although we also conducted transects over several rift-aligned tectonic faults in the vicinity of the edifice, none show elevated CO₂ flux or ground temperatures (Figure 9, B-B'). Previous work on Aluto volcano in the CMER (Hutchison et al., 2015) demonstrated the importance of localized permeability variations when trying to interpret diffuse CO₂ degassing. These localized variations may be associated with (a) changes in the surface lithology (Pantaleo & Walter, 2014), for example, where there are differences in permeability between dense obsidian lavas and unconsolidated pumice deposits, and (b) topographic controls on the stress field, where differences in surface loading focus permeable pathways toward topographic highs (Schöpa et al., 2011). At Aluto, high CO₂ flux values (100–1,000 g m⁻² d⁻¹) were often observed at topographic highs associated with piles of young volcanic deposits and indicated that the topography-induced stress field played a role focusing fluid pathways toward morphological crests (Hutchison et al., 2015). Our transects of the Salewa Dore-Hako rhyolitic center show similar correspondence between topography and CO₂ flux, and this leads us to infer a topographic control on the near-surface stress field. Our interpretation is that, like Aluto, there may be deep penetrating volcanic and/or tectonic structures which act as the main conduit of gas from depth, but once these gases enter the pile of unconsolidated volcanic material, the permeability pathways are mainly controlled by the topographic loading, and this ultimately determines the surface expression of gas emission.

5.2. Volcanic Gas Emissions: Origin and Magnitude

The bulk gases collected from fumaroles (in glass vials) are mainly dominated by N₂ and O₂ and represent air mixed with variable amounts of CO₂ (up to 36 mol.%). When we consider various sources for the CO₂

Figure 11. (a) Carbon isotopes ($\delta^{13}\text{C}$) of soil gas and fumarole samples from Ethiopian, Kenyan and Tanzania volcanic-hydrothermal systems. $\delta^{13}\text{C}$ of CO₂ is plotted against the reciprocal of CO₂ concentration in the sample. The data define a triangular array defined by three endmembers: air, biogenic CO₂ (with characteristic light $\delta^{13}\text{C}$ of -20‰ and -25‰) and magmatic CO₂ (with $\delta^{13}\text{C}$ between -3‰ and -8‰). (b) Inset of (a) showing $\delta^{13}\text{C}$ for the highest concentration samples (note the logarithmic rather than reciprocal scale). (c) He isotopes versus X -value. ${}^3\text{He}/{}^4\text{He}$ is corrected for air and given in R_c/R_A notation. The X -value is calculated as $({}^4\text{He}/{}^{20}\text{Ne})_{\text{measured}}/({}^4\text{He}/{}^{20}\text{Ne})_{\text{air}}$ and provides an assessment of how much air has been entrained into the sample. X -values close to 1 are air-dominated, and those with much higher X -values indicate that very little air has been incorporated into the sample. Endmember ${}^3\text{He}/{}^4\text{He}$ for depleted mid-ocean ridge basalts (MORB), subcontinental lithospheric mantle (SLCM), plume and crust are shown on the left of the plot after values from Gilfillan and Ballentine (2018), Bräuer et al. (2016), Hilton et al. (2011), Graham (2002), and Gautheron and Moreira (2002). Gas geochemical data from Ethiopia, Kenya and Tanzania are from Minissale et al. (2017), Hutchison et al. (2016), Darling (1998), Darrah et al. (2013), Muirhead et al. (2020), Barry et al. (2013), Kimani et al. (2021), and Mtili et al. (2021).

(Figure 11a), it becomes evident that their high CO₂ concentrations as well as δ¹³C values of −6.4‰ to −3.8‰, require a magmatic origin for the CO₂. The minor difference in CO₂ concentrations between our samples and those of Minissale et al. (2017) (Figure 11b) likely reflects minor differences in gas sampling setup (i.e., sealing of the sampling line and time spent flushing the line prior to sample collection). Crucially, the CO₂-δ¹³C values are almost identical to those of Minissale et al. (2017), who also concluded a mantle-derived magmatic origin.

He isotope samples provide additional insights into the origin of gases. New air-corrected He isotope (³He/⁴He) measurements range from 3.8 to 4.1 R_A. These values are lower than previously published values from Minissale et al. (2017), who observed a range of 4.4–7.5 R_A for all Abaya samples (Figure 11c). New data suggest that there may be a larger crustal contribution to gases collected in 2019. When taken together, He isotope values from the region overlap with the canonical range of mid-ocean ridge basalts (MORB) (8 ± 1, Graham, 2002) and SCLM (6.1 ± 2.1, cf. Bräuer et al., 2016; Day et al., 2015; Gautheron & Moreira, 2002; Gilfillan & Ballentine, 2018). Although the highest ³He/⁴He values from Abaya do imply a MORB source, we cannot exclude the possibility of SCLM contributions (given the overlapping values, Figure 11c). Moreover, the fact that we see a range of values scattered to low ³He/⁴He is suggestive of radiogenic ⁴He contributions from crustal sources (which have values of 0.02, Ozima & Podosek, 2002; Figure 11c). Given that thermal fluids sampled along the WAGF by Minissale et al. (2017) show clear evidence of water-rock interactions, it is very likely that groundwaters from crustal sources contribute radiogenic ⁴He. In short, the simplest explanation of the Abaya He isotope results is that they represent an upper mantle source with a crustal ⁴He overprint. This explains the scattered values and indeed similar scenarios have been proposed in other areas of immature rifting further south in the EARS (e.g., the Magadi and Natron basins in Kenya and Tanzania, Lee et al., 2017). A final observation from Abaya ³He/⁴He measurements is that they are very different from the plume influenced measurements from Dallol in Afar (after Darrah et al., 2013; Figure 11c). This supports geochemical evidence for a declining plume contribution SW along the MER (Rooney, Hanan, et al., 2012) and geophysical evidence for low-velocity anomalies focused beneath Afar and which have been linked to the African superplume (Bastow et al., 2010; Mulibo & Nyblade, 2013; Ritsema et al., 1999, 2011). Helium isotope data clearly support the interpretation of the MER as transition zone between upper mantle and lithospheric sources in the south and plume-influenced mantle in the north toward Afar.

As noted in Section 5.2, the WAGF and the intersecting fault network represent the deepest penetrating and most permeable area of North Abaya. CO₂ flux calculations support this and show that deep C emissions are focused along the WAGF which emits ~300 t d⁻¹ (10× the emissions from the flank of the rhyolitic complex, ~30 t d⁻¹, Figure 10). Although there are only a few CO₂ flux measurements from elsewhere in the EARS, it is evident that Abaya is an important C emitter; the flux is ~100× that of Longnot volcano in Kenya and ~3× that of the Oldoinyo Lengai summit area (Table 2). At Aluto volcano in the Central MER, Hutchison et al. (2015) measured CO₂ along a tectonic fault that dissects the volcanic edifice (Artu Jawe fault zone, Table 2) and found a CO₂ emission of ~60 t d⁻¹ over an area of 0.8 km². Scaling up these values, they calculated a total CO₂ flux from Aluto volcano of 250–500 t d⁻¹. This flux is of similar magnitude to that of Abaya, although we emphasize that while CO₂ emissions at Aluto are associated with numerous volcano-tectonic faults spread over an area of ~150 km², the CO₂ released from Abaya is focused along a single tectonic fault. The CO₂ flux density also shows similar values between the WAGF, the Artu Jawe fault zone on Aluto and other geothermal areas (e.g., Rotorua in New Zealand and Reykjanes geothermal area in Iceland, Table 2).

From a global perspective, the CO₂ emission from Abaya compares with complexes such as Vesuvius (Italy), El Chichon (Mexico) and Teide (Canary Islands), which all have active magmatic systems. More generally, estimates of CO₂ emissions from volcanoes with detectable SO₂ plumes (after Carn et al., 2017 and Fischer et al., 2019) suggest typical CO₂ fluxes between 100 and 300 kt yr⁻¹. Abaya's annual emission is ~110 kt yr⁻¹, which again underscores that even though Abaya does not represent a conventional volcanic edifice, the CO₂ emissions are comparable to the most active volcanic systems on Earth (Table 2). Taken together with the isotopic constraints (Figure 11), this implies that an active magmatic system must underlie Abaya. CO₂ emissions from a volcanic system are mainly a function of the mass and C content of the degassing magmatic source, and the permeability of the fracture network (Burton et al., 2013). While we cannot disentangle the role of source versus permeability in controlling CO₂ emissions, the equivalence of Abaya and Aluto (in terms of total flux and flux density, Table 1) is notable because it implies similarities in terms of magmatic heat sources and subsurface permeabilities. Given that Aluto represents a proven geothermal resource, this finding should encourage further exploration at Abaya.

Table 2

Comparison of CO₂ Flux for Different Volcanic and Geothermal Areas Ordered by CO₂ Flux Density (t km⁻² d⁻¹)

Study area	CO ₂ flux (t d ⁻¹)	Area (km ²)	CO ₂ flux density (t km ⁻² d ⁻¹)	Reference
East African Rift				
Abaya volcanic field, Ethiopia (Western Abaya graben boundary fault)	294	3.9	75	This study
Aluto, Ethiopia (Artu Jawe fault zone)	57	0.8	71	Hutchison et al. (2015)
Oldoinyo Lengai, Tanzania ^a	100	3.14	32	Koepenick et al. (1996)
Magadi-Natron Basin, Kenya and Tanzania	11,095	960	11	Lee et al. (2016)
Longonot volcano, Kenya	0.258	0.086	3	E. A. M. Robertson, Biggs, Cashman, et al. (2016)
Comparable geothermal fields				
Rotorua geothermal system, Taupo Volcanic Zone, New Zealand	620	8.9	70	Werner and Cardellini (2006)
Reykjanes geothermal area, Iceland	13.5	0.22	61	Fridriksson et al. (2006)
Yanbajain geothermal area, China	138	3.2	43	Chiodini et al. (1998)
Cordón de Inacaliri Volcanic Complex, Chile	0.53	0.0179	30	Marco et al. (2021)
Hengill Volcano, Iceland	1,526	168.1	9	P. A. Hernández et al. (2012)
Other volcanic systems				
Cerro Negro volcano, Nicaragua	2,800	0.58	4,828	Salazar et al. (2001)
Solfatara volcano, Italy	1,500	1	1,500	Chiodini et al. (2001)
El Chichón, Mexico (crater and crater lake)	370	0.308	1,200	Mazot et al. (2011)
Nea Kameni, Santorini, Greece (summit area) ^b	21–38	0.02	1,050–1,900	Parks et al. (2013)
Mammoth Mountain, Horseshoe Lake (flank area)	104.3	0.13	802	Cardellini et al. (2003)
Teide volcano, Spain (summit area)	380	0.53	717	P. A. Hernández et al. (1998)
Liu-Huang-Ku hydrothermal area, Taiwan (phreatic crater)	22.4	0.03	659	Lan et al. (2007)
Mud volcano, Yellowstone	1,730	3.5	494	Werner et al. (2000)
Hot Spring Basin, Yellowstone	60	0.16	387	Werner et al. (2008)
Methana volcanic system, Greece	2.59	0.01	259	D'Alessandro et al. (2008)
Hakkoda volcanic area, Japan (localized flank area)	127	0.58	219	P. Hernández et al. (2003)
Furnas volcano, São Miguel Island, Azores	968	5.2	186	Viveiros et al. (2010)
Miyakejima volcano, Japan (summit)	100–150	0.6	167	P. A. Hernández et al. (2001)
Planchón–Peteroa Volcanic Complex, Argentina and Chile	6.49	0.077	84	Lamberti et al. (2021)
Nisyros caldera, Greece	84	2	42	Cardellini et al. (2003)
Vulcano island, Italy (Western and Southern Slopes)	75	1.9	39	Chiodini et al. (1998)
Mount Epomeo, Italy (Western Flank)	32.6	0.86	38	Chiodini et al. (2004)
Iwojima volcano, Japan	760	22	35	Notsu et al. (2005)
Vesuvius, Italy	193.8	5.5	35	Froncini et al. (2004)
Cuicocha Caldera Lake, Ecuador	135	3.95	32	Sierra et al. (2021)
Satsuma-Iwojima volcano, Japan	80	2.5	32	Shimoike et al. (2002)
Pantelleria island, Italy	989	84	12	Favara et al. (2001)
Pululahua caldera, Ecuador	270	27.6	10	Padrón et al. (2008)

^aMeasurements assume CO₂ emission restricted to the summit and flank area with a diameter of 2 km. ^bMeasurements made across a period of volcanic unrest (Parks et al., 2013).

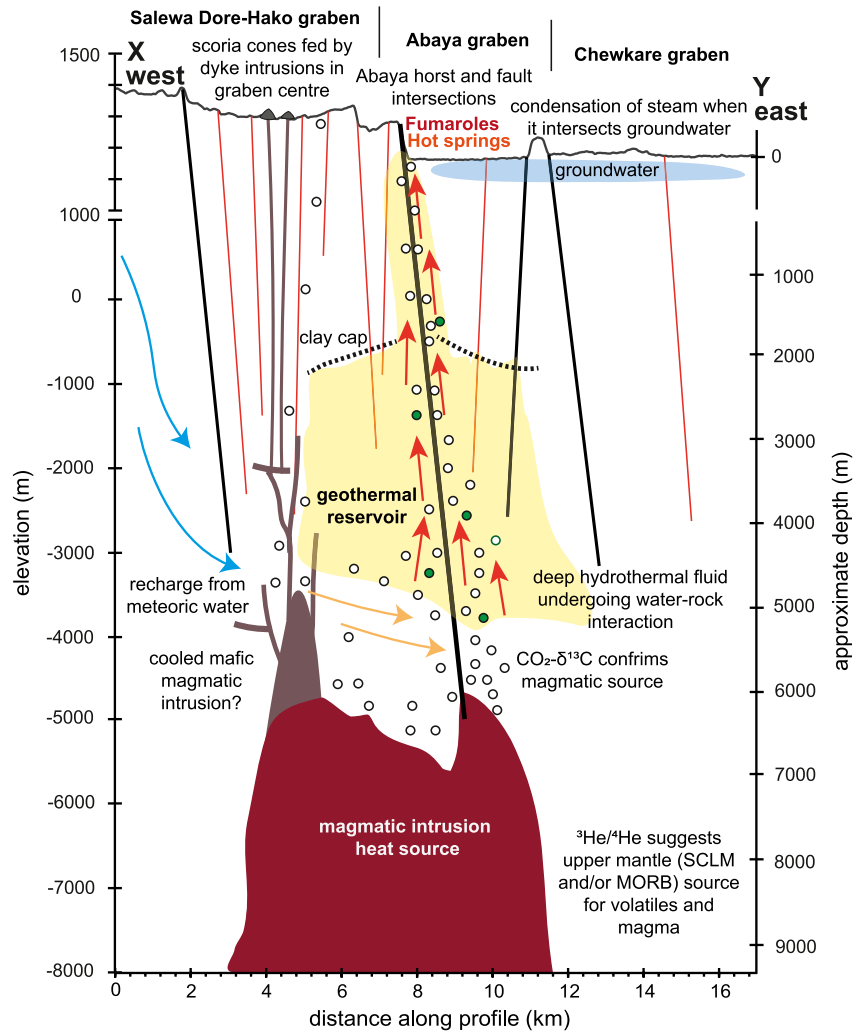


Figure 12. Schematic west-east cross section of the North Abaya geothermal system. The line of section corresponds to the profile X-Y shown in Figure 2. Arrows show directions of fluid flow and their color gives a qualitative indication of temperature. Deep magmatic intrusions are shown as red shaded areas. Gases are represented by circles: white circles indicate magmatic volatiles, green circles indicate crustal ^4He addition. The West Abaya graben fault is the key fault structure in the region and directs the flow of magmatic volatiles and hydrothermal fluids to the surface.

5.3. Architecture and Geothermal Potential

In Figure 12, we present a conceptual model of the North Abaya geothermal area based on our new measurements and the previous work of Chernet (2011), Corti et al. (2013) and Minissale et al. (2017). The heat for the geothermal field is sourced from magmatic intrusions and this is supported by the occurrence of recent, likely Holocene, volcanism in the area as well as our $\delta^{13}\text{C}$ and $^3\text{He}/^4\text{He}$ data and CO_2 flux constraints, which indicate a magmatic system originating from an upper mantle source (Figures 2 and 11). Hydrothermal fluids sampled from thermal springs at Abaya predominantly show a Na-HCO_3 composition and indicate significant water-rock interaction. Importantly, the oxygen ($\delta^{18}\text{O}$) and hydrogen (δD) isotopes of the Abaya hydrothermal fluids reveal a narrow range of values which parallel global and Addis Ababa meteoric water trends (Minissale et al., 2017). In contrast, surface waters from Lake Abaya and the Bilate and Humasa rivers show strong evaporation trends with positive enrichments in $\delta^{18}\text{O}$ and δD . These data demonstrate that the deep fluids circulating beneath Abaya are meteoric in origin and that there is no requirement for significant interactions with the highly evaporated lakes or surface water. The narrow $\delta^{18}\text{O}$ - δD range of the Abaya hydrothermal fluids implies a similar elevation (Minissale et al., 2017), and we suggest that the rift margin to the west of the geothermal field provides the most likely source area. It is worth noting that this finding is comparable to Aluto volcano, where $\delta^{18}\text{O}$ measurements also reveal

that despite proximity to major lakes, waters from the deep geothermal wells are meteoric in origin (>90%) and derived from rainfall on the rift margin (Darling et al., 1996; Rango et al., 2010).

The WAGF is the main tectonic structure in the North Abaya area. Its large ~110 m vertical offset is far greater than any of the other faults and indicates a wide fault damage zone (Section 5.1) and enhanced permeability (evidenced by the highest values of soil temperature and CO₂ flux, Figures 5 and 6). Field and remote sensing observations also indicate that this is a zone of fault intersection between the main graben bounding fault and other NNE-SSW regional faults (Figure 2b), which has led to a complex *en echelon* fabric as well as small-scale E-W faults (Figure 3b). In short, the WAGF constitutes the main upflow zone from the deep geothermal reservoir, and the numerous fault intersections amplify permeability (cf. Curewitz & Karson, 1997; Person et al., 2012) and concentrate fluid upflow at the tip of the Abaya horst (Figure 6).

One of the key uncertainties with our model is the architecture of the deep magmatic heat source (Figure 12). Although recent volcanism and hence magmatic intrusion appears to be focused in the Salewa Dore-Hako Graben, the main geothermal activity is offset from this and focused on the WAGF (where there is no evidence of recent volcanic activity). We suggest that the heat source is unlikely to be associated with the SDHRC because of its relatively small volume and location ~6 km north. We instead propose that the heat is sourced from a deeper mafic magma body (Figure 12) due to the fact that volcanism south of the Salewa Dore-Hako (nearest to the WAGF) is basaltic and indeed the formation of rhyolitic complexes necessitates large volumes of mafic intrusions (Hutchison et al., 2018). A similar setting to North Abaya may be the Butajira volcanic field in the CMER, which shows linear clusters of scoria cones within a marginal graben structure (Corti et al., 2018; Hunt et al., 2020). Here, a magnetotelluric study by Hübner et al. (2018) showed that the lines of scoria cones at the surface are horizontally offset from a deep conductive body at ~5–10 km depth, which can be interpreted as mafic melt. We speculate that there may be an analogous situation at North Abaya where the main magmatic intrusion (and heat source for the geothermal system) is centered on the Abaya graben but volcanic activity is horizontally offset and concentrated along dyke intrusions in the Salewa Dore-Hako graben (Figure 12).

To date, most studies of East African geothermal plays have focused on silicic caldera complexes (Gianelli & Teklemariam, 1993; Hochstein et al., 2017; Hutchison et al., 2015; Omenda, 1998). Magnetotellurics has proved particularly powerful at imaging geothermal resources, and at Aluto and Tulu Moyo (Ethiopia) these data often suggest the presence of a shallow high conductivity clay cap layer overlying a low conductivity pressurized hydrothermal system (Hübner et al., 2018; Samrock et al., 2015, 2018). Magnetotellurics has been conducted at North Abaya by Reykjavik Geothermal and support the occurrence of a high conductivity clay cap rock at a depth of 0.5–2 km (Eysteinnsson, pers. comm.). This is shown schematically in Figure 12 and we speculate that the WAGF provides the only major zone of permeability through this cap layer (hence why fumaroles, hot springs and degassing anomalies are largely restricted to this deep penetrating structure).

A final observation of the North Abaya geothermal area is that unlike the silicic volcanic complexes of Tulu Moyo and Aluto, there have been no episodes of ground deformation detected over a period spanning 1993 to 2020 (Biggs et al., 2011; Albino & Biggs, 2021; Albino et al., 2022; Figure 4). At Tulu Moyo, deformation has been linked to large-scale pressurization of the magmatic system, while at Aluto, seasonal uplift-subsidence patterns related to rainfall and pore pressure changes of the hydrothermal system are superimposed on longer-term magmatic-hydrothermal pressurization (Braddock et al., 2017; Hutchison et al., 2016). The fact that North Abaya displays neither of these trends demonstrates that (a) there have been no detectable magmatic intrusions, and (b) the geothermal reservoir does not respond to seasonal variations in rainfall. These data suggest that the mafic magmatic heat source beneath Abaya is less active and restless than the silicic mush systems of Tulu Moyo and Aluto, it also suggests that the geothermal reservoir is potentially much larger than these other systems, or that timescales of groundwater flow between meteoric source and the heat source are much slower (such that seasonal variations in pore pressure are not observed). Ultimately, the lack of surface volcanism and ground deformation along the WAGF stands in stark contrast to the restless silicic calderas elsewhere in the MER (Albino & Biggs, 2021; Biggs et al., 2011), and while further monitoring of the prospect is essential, this does make it an attractive system for further exploration and development.

6. Conclusions and Future Opportunities

We have combined remote sensing, soil CO₂ and ground temperature surveys and gas chemistry analysis to build up a detailed understanding of the North Abaya geothermal system in the SMER. The main outcomes of our study are:

1. the North Abaya region displays a horst-graben morphology, and graben bounding faults represent the deepest penetrating, most permeable structures,
2. soil CO₂ flux and temperatures reveal that the most permeable structure is the WAGF, and that deep hydrothermal upflow is concentrated along this structure and into a zone of fault intersections,
3. even though there is no surface volcanism along the WAGF, gas emissions are ~300 t d⁻¹ and comparable to average values from the world's subaerial volcanoes (e.g., Vesuvius, Teide, El Chichon, Table 2),
4. gas emissions require an active magmatic system, and new C- and He-isotopes suggest an upper mantle source (SCLM and/or MORB) that is overprinted by crustal ⁴He additions.

Our work presents the first detailed conceptual model of a fault-controlled magmatic geothermal resource in East Africa (Figure 12). Further refinement and testing of our conceptual model will require additional geophysical and geochemical surveys of the WAGF. These would include focused seismic and magnetotelluric surveys to better understand the distribution of melt, geothermal fluids, and gases in the subsurface, and the orientation of fracture sets beneath the fault zone (e.g., Nowacki et al., 2018; Samrock et al., 2018; Wilks et al., 2020). Further geochemical investigations should consider measuring radon and thoron, which can provide insights into depths and speeds of geothermal upflow (Jolie et al., 2019), and additional CO₂-δ¹³C would allow us to determine whether the different background populations inferred from log-probability plots (Section 4.3, Figure 7) show different isotopic fingerprints therefore requiring different sources.

North Abaya is a very promising site for geothermal development and in particular the northern tip of the Abaya horst, where ground temperature is highest, and permeability is enhanced by multiple intersecting faults. Compared to the active silicic caldera volcanoes that are generally seen as East Africa's best geothermal prospects, the WAGF shows no evidence of ground deformation or recent volcanism. While there are still risks of volcanic and tectonic hazards in the North Abaya area, and monitoring is to be encouraged, we suggest that fault-controlled geothermal plays, linked to deep mafic magma body sources, could represent safer and more sustainable prospects than silicic caldera volcanoes.

Data Availability Statement

All data produced during this study are provided in Data Set S1. The research data can also be accessed at <https://doi.org/10.17630/ec8c0a17-eb2c-49c7-ab06-9e59b6fb678a>.

References

- Acocella, V., Korme, T., Salvini, F., & Funicello, R. (2003). Elliptic calderas in the Ethiopian Rift: Control of pre-existing structures. *Journal of Volcanology and Geothermal Research*, 119(1–4), 189–203. [https://doi.org/10.1016/S0377-0273\(02\)00342-6](https://doi.org/10.1016/S0377-0273(02)00342-6)
- Agostini, A., Bonini, M., Corti, G., Sani, F., & Mazzarini, F. (2011). Fault architecture in the Main Ethiopian Rift and comparison with experimental models: Implications for rift evolution and Nubia-Somalia kinematics. *Earth and Planetary Science Letters*, 301(3–4), 479–492. <https://doi.org/10.1016/j.epsl.2010.11.024>
- Agusto, M., Tassi, F., Caselli, A. T., Vaselli, O., Rouwet, D., Capaccioni, B., et al. (2013). Gas geochemistry of the magmatic-hydrothermal fluid reservoir in the Copahue-Caviahue Volcanic Complex (Argentina). *Journal of Volcanology and Geothermal Research*, 257, 44–56. <https://doi.org/10.1016/j.jvolgeores.2013.03.003>
- Albino, F., & Biggs, J. (2021). Magmatic processes in the East African Rift System: Insights from a 2015–2020 Sentinel-1 InSAR survey. *Geochemistry, Geophysics, Geosystems*, 22(3), 1–24. <https://doi.org/10.1029/2020GC009488>
- Albino, F., Biggs, J., Lazecký, M., & Maghsoudi, Y. (2022). Routine processing and automatic detection of volcanic ground deformation using Sentinel-1 InSAR data: Insights from African volcanoes. *Remote Sensing*, 14(22), 5703. <https://doi.org/10.3390/rs14225703>
- Barry, P. H., Hilton, D. R., Fischer, T. P., de Moor, J. M., Mangasini, F., & Ramirez, C. (2013). Helium and carbon isotope systematics of cold “mazuku” CO₂ vents and hydrothermal gases and fluids from Rungwe Volcanic Province, southern Tanzania. *Chemical Geology*, 339(July), 141–156. <https://doi.org/10.1016/j.chemgeo.2012.07.003>
- Barry, P. H., Lawson, M., Meurer, W. P., Warr, O., Mabry, J. C., Byrne, D. J., & Ballentine, C. J. (2016). Noble gases solubility models of hydrocarbon charge mechanism in the Sleiþner Vest gas field. *Geochimica et Cosmochimica Acta*, 194, 291–309. <https://doi.org/10.1016/j.gca.2016.08.021>
- Bastow, I. D., Pilidou, S., Kendall, J., & Stuart, G. W. (2010). Melt-induced seismic anisotropy and magma assisted rifting in Ethiopia: Evidence from surface waves. *Geochemistry, Geophysics, Geosystems*, 11(6). <https://doi.org/10.1029/2010gc003036>
- Bense, V. F., Gleeson, T., Loveless, S. E., Bour, O., & Scibek, J. (2013). Fault zone hydrogeology. *Earth-Science Reviews*, 127, 171–192. <https://doi.org/10.1016/j.earscirev.2013.09.008>

Acknowledgments

W. Hutchison is funded by a UKRI Future Leaders Fellowship (MR/S033505/1). E.R.D. Ogilvie was supported by a St Andrews Research Internship Scheme (StARIS) grant from the University of St Andrews. Fátima Viveiros and Giacomo Corti provided constructive reviews that helped improve the manuscript.

- Benvenuti, M., Corti, G., Keir, D., & Sani, F. (2023). Transverse tectonics control on the late quaternary development of the Central main Ethiopian rift. *Italian Journal of Geoscience*, 142(1), 42–56. <https://doi.org/10.3301/IJG.2023.05>
- Biggs, J., Anthony, E. Y., & Ebinger, C. J. (2009). Multiple inflation and deflation events at Kenyan volcanoes, East African Rift. *Geology*, 37(11), 979–982. <https://doi.org/10.1130/G30133A.1>
- Biggs, J., Ayele, A., Fischer, T. P., Fontijn, K., Hutchison, W., Kazimoto, E., et al. (2021). Volcanic activity and hazard in the East African Rift Zone. *Nature Communications*, 12(1), 1–12. <https://doi.org/10.1038/s41467-021-27166-y>
- Biggs, J., Bastow, I. D., Keir, D., & Lewi, E. (2011). Pulses of deformation reveal frequently recurring shallow magmatic activity beneath the Main Ethiopian Rift. *Geochemistry, Geophysics, Geosystems*, 12(9). <https://doi.org/10.1029/2011gc003662>
- Birhanu, Y., Wilks, M., Biggs, J., Kendall, J., Ayele, A., & Lewi, E. (2018). Seasonal patterns of seismicity and deformation at the Alutu geothermal reservoir, Ethiopia, induced by hydrological loading. *Journal of Volcanology and Geothermal Research*, 356, 175–182. <https://doi.org/10.1016/j.jvolgeoes.2018.03.008>
- Boccaletti, M., Mazzuoli, R., Bonini, M., Trua, T., & Abebe, B. (1999). Plio-Quaternary volcanotectonic activity in the northern sector of the Main Ethiopian Rift: Relationships with oblique rifting. *Journal of African Earth Sciences*, 29(4), 679–698. [https://doi.org/10.1016/S0899-5362\(99\)00124-4](https://doi.org/10.1016/S0899-5362(99)00124-4)
- Braddock, M., Biggs, J., Watson, I. M., Hutchison, W., Pyle, D. M., & Mather, T. A. (2017). Satellite observations of fumarole activity at Alutu volcano, Ethiopia: Implications for geothermal monitoring and volcanic hazard. *Journal of Volcanology and Geothermal Research*, 341, 70–83. <https://doi.org/10.1016/j.jvolgeoes.2017.05.006>
- Bräuer, K., Geissler, W. H., Kämpf, H., Niedermann, S., & Rman, N. (2016). Helium and carbon isotope signatures of gas exhalations in the westernmost part of the Pannonian Basin (SE Austria/NE Slovenia): Evidence for active lithospheric mantle degassing. *Chemical Geology*, 422, 60–70. <https://doi.org/10.1016/j.chemgeo.2015.12.016>
- Burnside, N., Montcoudiol, N., Becker, K., & Lewi, E. (2021). Geothermal energy resources in Ethiopia: Status review and insights from hydrochemistry of surface and groundwaters. *Wiley Interdisciplinary Reviews: Water*, 8(6), 1–27. <https://doi.org/10.1002/wat2.1554>
- Burton, M. R., Sawyer, G. M., & Granieri, D. (2013). Deep carbon emissions from volcanoes. *Reviews in Mineralogy and Geochemistry*, 75(1), 323–354. <https://doi.org/10.2138/rmg.2013.75.11>
- Carapezza, M. L., & Granieri, D. (2004). CO₂ soil flux at Vulcano (Italy): Comparison between active and passive methods. *Applied Geochemistry*, 19(1), 73–88. [https://doi.org/10.1016/S0883-2927\(03\)00111-2](https://doi.org/10.1016/S0883-2927(03)00111-2)
- Cardellini, C., Chioldini, G., & Frondini, F. (2003). Application of stochastic simulation to CO₂ flux from soil: Mapping and quantification of gas release. *Journal of Geophysical Research*, 108(B9), 2425. <https://doi.org/10.1029/2002jb002165>
- Carn, S. A., Fioletov, V. E., McLinden, C. A., Li, C., & Krotkov, N. A. (2017). A decade of global volcanic SO₂ emissions measured from space. *Scientific Reports*, 7, 1–12. <https://doi.org/10.1038/srep44095>
- Casey, M., Ebinger, C. J., Keir, D., Gloaguen, R., & Mohamed, F. (2006). *Strain accommodation in transitional rifts: Extension by magma intrusion and faulting in Ethiopian rift magmatic segments* (Vol. 259, pp. 143–163). Geological Society Special Publication. <https://doi.org/10.1144/GSL.SP.2006.259.01.13>
- Cheng, W. (1996). Measurement of rhizosphere respiration and organic matter decomposition using natural ¹³C. *Plant and Soil*, 183(2), 263–268. <https://doi.org/10.1007/bf00011441>
- Chernet, T. (2011). Geology and hydrothermal resources in the northern Lake Abaya area (Ethiopia). *Journal of African Earth Sciences*, 61(2), 129–141. <https://doi.org/10.1016/j.jafrearsci.2011.05.006>
- Chioldini, G., Avino, R., Brombach, T., Caliro, S., Cardellini, C., De Vita, S., et al. (2004). Fumarolic and diffuse soil degassing west of Mount Epomeo, Ischia, Italy. *Journal of Volcanology and Geothermal Research*, 133(1–4), 291–309. [https://doi.org/10.1016/S0377-0273\(03\)00403-7](https://doi.org/10.1016/S0377-0273(03)00403-7)
- Chioldini, G., Caliro, S., Cardellini, C., Avino, R., Granieri, D., & Schmidt, A. (2008). Carbon isotopic composition of soil CO₂ efflux, a powerful method to discriminate different sources feeding soil CO₂ degassing in volcanic-hydrothermal areas. *Earth and Planetary Science Letters*, 274(3–4), 372–379. <https://doi.org/10.1016/j.epsl.2008.07.051>
- Chioldini, G., Cioni, R., Guidi, M., Raco, B., & Marini, L. (1998). Soil CO₂ flux measurements in volcanic and geothermal areas. *Applied Geochemistry*, 13(5), 543–552. [https://doi.org/10.1016/S0883-2927\(97\)00076-0](https://doi.org/10.1016/S0883-2927(97)00076-0)
- Chioldini, G., Frondini, F., Cardellini, C., Granieri, D., Marini, L., & Ventura, G. G. (2001). CO₂ degassing and energy release at Solfatara volcano, Campi Flegrei, Italy. *Journal of Geophysical Research*, 106(B8), 9–16221. <https://doi.org/10.1029/2001jb000246>
- Choi, J.-H., Edwards, P., Ko, K., & Kim, Y.-S. (2016). Definition and classification of fault damage zones: A review and a new methodological approach. *Earth-Science Reviews*, 152, 70–87. <https://doi.org/10.1016/j.earscirev.2015.11.006>
- Clarke, B., Tierz, P., Calder, E., & Yirgu, G. (2020). Probabilistic volcanic hazard assessment for pyroclastic density currents from pumice Cone eruptions at Alutu volcano, Ethiopia. *Frontiers of Earth Science*, 8(August), 1–19. <https://doi.org/10.3389/feart.2020.00348>
- Corti, G. (2009). Continental rift evolution: From rift initiation to incipient break-up in the Main Ethiopian Rift, East Africa. *Earth-Science Reviews*, 96(1–2), 1–53. <https://doi.org/10.1016/j.earscirev.2009.06.005>
- Corti, G., Molin, P., Sembroni, A., Bastow, I. D., & Keir, D. (2018). Control of pre-rift lithospheric structure on the architecture and evolution of Continental rifts: Insights from the Main Ethiopian Rift, East Africa. *Tectonics*, 37(2), 477–496. <https://doi.org/10.1002/2017TC004799>
- Corti, G., Sani, F., Philippon, M., Sokoutis, D., Willingshofer, E., & Molin, P. (2013). Quaternary volcano-tectonic activity in the Soddo region, western margin of the southern main Ethiopian rift. *Tectonics*, 32(4), 861–879. <https://doi.org/10.1002/tect.20052>
- Craig, H., Lupton, J. E., & Horowitz, R. M. (1977). *Isotope geochemistry and hydrology of geothermal waters in the Ethiopian Rift Valley*. Scripps Institution of Oceanography.
- Curewitz, D., & Karson, J. A. (1997). Structural settings of hydrothermal outflow: Fracture permeability maintained by fault propagation and interaction. *Journal of Volcanology and Geothermal Research*, 79(3–4), 149–168. [https://doi.org/10.1016/S0377-0273\(97\)00027-9](https://doi.org/10.1016/S0377-0273(97)00027-9)
- D'Alessandro, W., Brusca, L., Kyriakopoulos, K., Michas, G., & Papadakis, G. (2008). Methana, the westernmost active volcanic system of the south Aegean arc (Greece): Insight from fluids geochemistry. *Journal of Volcanology and Geothermal Research*, 178(4), 818–828. <https://doi.org/10.1016/j.jvolgeoes.2008.09.014>
- Darling, W. G. (1998). Hydrothermal hydrocarbon gases: 2, application in the East African Rift System. *Applied Geochemistry*, 13(7), 825–840. [https://doi.org/10.1016/S0883-2927\(98\)00022-5](https://doi.org/10.1016/S0883-2927(98)00022-5)
- Darling, W. G., Gizaw, B., & Arusei, M. K. (1996). Lake-groundwater relationships and fluid-rock interaction in the East African rift valley: Isotopic evidence. *Journal of African Earth Sciences*, 22(4), 423–431. [https://doi.org/10.1016/0899-5362\(96\)00026-7](https://doi.org/10.1016/0899-5362(96)00026-7)
- Darling, W. G., Griesshaber, E., Andrews, J. N., Armannsson, H., & O'Nions, R. K. (1995). The origin of hydrothermal and other gases in the Kenya Rift Valley. *Geochimica et Cosmochimica Acta*, 59(12), 2501–2512. [https://doi.org/10.1016/0016-7037\(95\)00145-X](https://doi.org/10.1016/0016-7037(95)00145-X)
- Darrah, T. H., Tedesco, D., Tassi, F., Vaselli, O., Cuoco, E., & Poreda, R. J. (2013). Gas chemistry of the Dallol region of the Danakil depression in the Afar region of the northern-most East African Rift. *Chemical Geology*, 339, 16–29. <https://doi.org/10.1016/j.chemgeo.2012.10.036>

- Day, J. M. D., Barry, P. H., Hilton, D. R., Burgess, R., Pearson, D. G., & Taylor, L. A. (2015). The helium flux from the continents and ubiquity of low-³He/⁴He recycled crust and lithosphere. *Geochimica et Cosmochimica Acta*, *153*, 116–133. <https://doi.org/10.1016/j.gca.2015.01.008>
- Deutsch, C. V., & Journel, A. G. (1998). *GSLIB: Geostatistical software library and user's guide* (2nd ed.). Oxford University Press. <https://doi.org/10.1017/s0016756899531774>
- Ebinger, C. J. (2005). Continental break-up: The East African perspective. *Astronomy and Geophysics*, *46*(2), 2-16–2-21. <https://doi.org/10.1111/j.1468-4004.2005.46216.x>
- Ebinger, C. J., & Casey, M. (2001). Continental breakup in magmatic provinces: An Ethiopian example. *Geology*, *29*(6), 527–530. [https://doi.org/10.1130/0091-7613\(2001\)029<0527:CBIMPA>2.0.CO;2](https://doi.org/10.1130/0091-7613(2001)029<0527:CBIMPA>2.0.CO;2)
- Faulkner, D. R., Mitchell, T. M., Jensen, E., & Cembrano, J. (2011). Scaling of fault damage zones with displacement and the implications for fault growth processes. *Journal of Geophysical Research*, *116*(B5), B05403. <https://doi.org/10.1029/2010jb007788>
- Favara, R., Giammanco, S., Inguaggiato, S., & Pecoraino, G. (2001). Preliminary estimate of CO₂ output from Pantelleria Island volcano (Sicily, Italy): Evidence of active mantle degassing. *Applied Geochemistry*, *16*(7–8), 883–894. [https://doi.org/10.1016/S0883-2927\(00\)00055-X](https://doi.org/10.1016/S0883-2927(00)00055-X)
- Fischer, T. P., Arellano, S., Carn, S., Aiuppa, A., Galle, B., Allard, P., et al. (2019). The emissions of CO₂ and other volatiles from the world's subaerial volcanoes. *Scientific Reports*, *9*(1), 1–11. <https://doi.org/10.1038/s41598-019-54682-1>
- Fontijn, K., McNamara, K., Zafu Tadesse, A., Pyle, D. M., Dessalegn, F., Hutchison, W., et al. (2018). Contrasting styles of post-caldera volcanism along the Main Ethiopian Rift: Implications for contemporary volcanic hazards. *Journal of Volcanology and Geothermal Research*, *356*, 90–113. <https://doi.org/10.1016/j.jvolgeores.2018.02.001>
- Fridriksson, T., Kristjánsson, B. R., Ármannsson, H., Margrétardóttir, E., Ólafsdóttir, S., & Chiodini, G. (2006). CO₂ emissions and heat flow through soil, fumaroles, and steam heated mud pools at the Reykjanes geothermal area, SW Iceland. *Applied Geochemistry*, *21*(9), 1551–1569. <https://doi.org/10.1016/j.apgeochem.2006.04.006>
- Fronzoni, F., Chiodini, G., Caliro, S., Cardellini, C., Granieri, D., & Ventura, G. (2004). Diffuse CO₂ degassing at Vesuvio, Italy. *Bulletin of Volcanology*, *66*(7), 642–651. <https://doi.org/10.1007/s00445-004-0346-x>
- Gautheron, C., & Moreira, M. (2002). Helium signature of the subcontinental lithospheric mantle. *Earth and Planetary Science Letters*, *199*(1–2), 39–47. [https://doi.org/10.1016/S0012-821X\(02\)00563-0](https://doi.org/10.1016/S0012-821X(02)00563-0)
- Gerlach, T. M., & Taylor, B. E. (1990). Carbon isotope constraints on degassing of carbon dioxide from Kilauea Volcano. *Geochimica et Cosmochimica Acta*, *54*(7), 2051–2058. [https://doi.org/10.1016/0016-7037\(90\)90270-u](https://doi.org/10.1016/0016-7037(90)90270-u)
- Giammanco, S., Parello, F., Gambardella, B., Schifano, R., Pizzullo, S., & Galante, G. (2007). Focused and diffuse effluxes of CO₂ from mud volcanoes and mofettes south of Mt. Etna (Italy). *Journal of Volcanology and Geothermal Research*, *165*(1–2), 46–63. <https://doi.org/10.1016/j.jvolgeores.2007.04.010>
- Gianelli, G., & Teklemariam, M. (1993). Water-rock interaction processes in the Aluto-Langano geothermal field (Ethiopia). *Journal of Volcanology and Geothermal Research*, *56*(4), 429–445. [https://doi.org/10.1016/0377-0273\(93\)90007-E](https://doi.org/10.1016/0377-0273(93)90007-E)
- Gibson, I. L. (1969). The structure and volcanic geology of an axial portion of the Main Ethiopian Rift. *Tectonophysics*, *8*(4–6), 561–565. [https://doi.org/10.1016/0040-1951\(69\)90054-7](https://doi.org/10.1016/0040-1951(69)90054-7)
- Gilfillan, S. M. V., & Ballentine, C. J. (2018). He, Ne and Ar 'snapshot' of the subcontinental lithospheric mantle from CO₂ well gases. *Chemical Geology*, *480*(September 2017), 116–127. <https://doi.org/10.1016/j.chemgeo.2017.09.028>
- Gleeson, M. L. M., Stock, M. J., Pyle, D. M., Mather, T. A., Hutchison, W., Yirgu, G., & Wade, J. (2017). Constraining magma storage conditions at a restless volcano in the Main Ethiopian Rift using phase equilibria models. *Journal of Volcanology and Geothermal Research*, *337*, 44–61. <https://doi.org/10.1016/j.jvolgeores.2017.02.026>
- Graham, D. W. (2002). Noble gas isotope geochemistry of mid-ocean ridge and ocean island basalts: Characterization of mantle source reservoirs. *Reviews in Mineralogy and Geochemistry*, *47*(1), 247–317. <https://doi.org/10.2138/rmg.2002.47.8>
- Hernández, P., Notsu, K., Tsurumi, M., Mori, T., Ohno, M., Shimoike, Y., et al. (2003). Carbon dioxide emissions from soils at Hakkoda, north Japan. *Journal of Geophysical Research*, *108*(B4), 1–10. <https://doi.org/10.1029/2002jb001847>
- Hernández, P. A., Pérez, N. M., Fridriksson, T., Egbert, J., Ilyinskaya, E., Thárhallsson, A., et al. (2012). Diffuse volcanic degassing and thermal energy release from Hengill volcanic system, Iceland. *Bulletin of Volcanology*, *74*(10), 2435–2448. <https://doi.org/10.1007/s00445-012-0673-2>
- Hernández, P. A., Pérez, N. M., Salazar, J. M., Nakai, S., Notsu, K., & Wakita, H. (1998). Diffuse emission of carbon dioxide, methane, and helium-3 from Teide Volcano, Tenerife, Canary Islands. *Geophysical Research Letters*, *25*(17), 3311–3314. <https://doi.org/10.1029/98GL02561>
- Hernández, P. A., Salazar, J. M., Shimoike, Y., Mori, T., Notsu, K., & Pérez, N. (2001). Diffuse emission of CO₂ from Miyakejima Volcano, Japan. *Chemical Geology*, *177*(1–2), 175–185. [https://doi.org/10.1016/S0009-2541\(00\)00390-9](https://doi.org/10.1016/S0009-2541(00)00390-9)
- Hilton, D. R. (1996). The helium and carbon isotope systematics of a continental geothermal system: Results from monitoring studies at Long Valley caldera (California, U.S.A.). *Chemical Geology*, *127*(4), 269–295. [https://doi.org/10.1016/0009-2541\(95\)00134-4](https://doi.org/10.1016/0009-2541(95)00134-4)
- Hilton, D. R., Halldórsson, S. A., Barry, P. H., Fischer, T. P., De Moor, J. M., Ramirez, C. J., et al. (2011). Helium isotopes at Rungwe Volcanic Province, Tanzania, and the origin of East African Plateaux. *Geophysical Research Letters*, *38*(21), 1–5. <https://doi.org/10.1029/2011GL049589>
- Hochstein, M. P., Oluma, B., & Hole, H. (2017). Early exploration of the Aluto geothermal field, Ethiopia (History of discovery well LA-3). *Geothermics*, *66*, 73–84. <https://doi.org/10.1016/j.geothermics.2016.11.010>
- Hübert, J., Whaler, K., & Fisseha, S. (2018). The electrical structure of the central main Ethiopian Rift as imaged by magnetotellurics: Implications for magma storage and pathways. *Journal of Geophysical Research: Solid Earth*, *123*(7), 6019–6032. <https://doi.org/10.1029/2017JB015160>
- Hunt, J. A., Mather, T. A., & Pyle, D. M. (2020). Morphological comparison of distributed volcanic fields in the Main Ethiopian Rift using high-resolution digital elevation models. *Journal of Volcanology and Geothermal Research*, *393*, 106732. <https://doi.org/10.1016/j.jvolgeores.2019.106732>
- Hunt, J. A., Pyle, D. M., & Mather, T. A. (2019). The geomorphology, structure, and lava flow dynamics of peralkaline rift volcanoes from high-resolution digital elevation models. *Geochemistry, Geophysics, Geosystems*, *20*(3), 1508–1538. <https://doi.org/10.1029/2018GC008085>
- Hunt, J. A., Zafu, A., Mather, T. A., Pyle, D. M., & Barry, P. H. (2017). Spatially variable CO₂ degassing in the Main Ethiopian Rift: Implications for magma storage, volatile transport, and rift-related emissions. *Geochemistry, Geophysics, Geosystems*, *18*(10), 3714–3737. <https://doi.org/10.1002/2017GC006975>
- Hutchison, W., Biggs, J., Mather, T. A., Pyle, D. M., Lewi, E., Yirgu, G., et al. (2016). Causes of unrest at silicic calderas in the East African Rift: New constraints from InSAR and soil-gas chemistry at Aluto volcano, Ethiopia. *Geochemistry, Geophysics, Geosystems*, *17*(8), 3008–3030. <https://doi.org/10.1002/2016GC006395>
- Hutchison, W., Mather, T. A., Pyle, D. M., Biggs, J., & Yirgu, G. (2015). Structural controls on fluid pathways in an active rift system: A case study of the Aluto volcanic complex. *Geosphere*, *11*(3), 542–562. <https://doi.org/10.1130/GES01119.1>
- Hutchison, W., Mather, T. A., Pyle, D. M., Boyce, A. J., Gleeson, M. L. M., Yirgu, G., et al. (2018). The evolution of magma during continental rifting: New constraints from the isotopic and trace element signatures of silicic magmas from Ethiopian volcanoes. *Earth and Planetary Science Letters*, *489*, 203–218. <https://doi.org/10.1016/j.epsl.2018.02.027>

- Iddon, F., & Edmonds, M. (2020). Volatile-rich magmas distributed through the upper crust in the Main Ethiopian Rift. *Geochemistry, Geophysics, Geosystems*, 21(6), e2019GC008904. <https://doi.org/10.1029/2019GC008904>
- Iddon, F., Jackson, C., Hutchison, W., Fontijn, K., Pyle, D. M., Mather, T. A., et al. (2019). Mixing and crystal scavenging in the Main Ethiopian Rift revealed by trace element systematics in feldspars and glasses. *Geochemistry, Geophysics, Geosystems*, 20(1), 230–259. <https://doi.org/10.1029/2018GC007836>
- Javoy, M., & Pineau, F. (1991). The volatiles record of a “popping” rock from the Mid-Atlantic Ridge at 14 N: Chemical and isotopic composition of gas trapped in the vesicles. *Earth and Planetary Science Letters*, 107(3–4), 598–611. [https://doi.org/10.1016/0012-821x\(91\)90104-p](https://doi.org/10.1016/0012-821x(91)90104-p)
- Jolie, E., Hutchison, W., Driba, D. L., Jentsch, A., & Gizaw, B. (2019). Pinpointing deep geothermal upflow in zones of complex tectono-volcanic degassing: New insights from Aluto Volcano, Main Ethiopian Rift. *Geochemistry, Geophysics, Geosystems*, 20(8), 4146–4161. <https://doi.org/10.1029/2019GC008309>
- Keir, D., Ebinger, C. J., Stuart, G. W., Daly, E., & Ayele, A. (2006). Strain accommodation by magmatism and faulting as rifting proceeds to breakup: Seismicity of the northern Ethiopian rift. *Journal of Geophysical Research*, 111(5), 1–17. <https://doi.org/10.1029/2005JB003748>
- Kendall, J. M., Stuart, G. W., Ebinger, C. J., Bastow, I. D., & Keir, D. (2005). Magma-assisted rifting in Ethiopia. *Nature*, 433(7022), 146–148. <https://doi.org/10.1038/nature03161>
- Kennedy, B. M., Lynch, M. A., Reynolds, J. H., & Smith, S. P. (1985). Intensive sampling of noble gases in fluids at Yellowstone: I. Early overview of the data; regional patterns. *Geochimica et Cosmochimica Acta*, 49(5), 1251–1261. [https://doi.org/10.1016/0016-7037\(85\)90014-6](https://doi.org/10.1016/0016-7037(85)90014-6)
- Kimani, C. N., Kasanzu, C. H., Tyne, R. L., Mtili, K. M., Byrne, D. J., Kazimoto, E. O., et al. (2021). He, Ne, Ar and CO₂ systematics of the Rungwe Volcanic Province, Tanzania: Implications for fluid source and dynamics. *Chemical Geology*, 586(July), 120584. <https://doi.org/10.1016/j.chemgeo.2021.120584>
- Knott, S. D., Beach, A., Brockbank, P. J., Brown, J. L., McCallum, J. E., & Welbon, A. I. (1996). Spatial and mechanical controls on normal fault populations. *Journal of Structural Geology*, 18(2–3), 359–372. [https://doi.org/10.1016/s0191-8141\(96\)80056-3](https://doi.org/10.1016/s0191-8141(96)80056-3)
- Koepenick, K. W., Brantley, S. L., Thompson, J. M., Rowe, G. L., Nyblade, A. A., & Moshy, C. (1996). Volatile emissions from the crater and flank of Oldoinyo Lengai volcano, Tanzania. *Journal of Geophysical Research*, 101(6), 13819–13830. <https://doi.org/10.1029/96jb00173>
- Kogan, L., Fisseha, S., Bendick, R., Reilinger, R., McClusky, S., King, R., & Solomon, T. (2012). Lithospheric strength and strain localization in continental extension from observations of the East African Rift. *Journal of Geophysical Research*, 117(3), 1–16. <https://doi.org/10.1029/2011JB008516>
- Kombe, E. Y., & Muguthu, J. (2018). Geothermal energy development in East Africa: Barriers and strategies. *Journal of Energy Research and Reviews*, 2, 1–6. <https://doi.org/10.9734/jenrr/2019/v2i129722>
- Lamberti, M. C., Agosto, M., Llano, J., Nogués, V., Venturi, S., Vélez, M. L., et al. (2021). Soil CO₂ flux baseline in Planchón–Petroa Volcanic Complex, Southern Andes, Argentina-Chile. *Journal of South American Earth Sciences*, 105, 102930. <https://doi.org/10.1016/j.jsames.2020.102930>
- Lan, T. F., Yang, T. F., Lee, H. F., Chen, Y. G., Chen, C. H., Song, S. R., & Tsao, S. (2007). Compositions and flux of soil gas in Liu-Huang-Ku hydrothermal area, northern Taiwan. *Journal of Volcanology and Geothermal Research*, 165(1–2), 32–45. <https://doi.org/10.1016/j.jvolgeores.2007.04.015>
- Lee, H., Fischer, T. P., Muirhead, J. D., Ebinger, C. J., Kattenhorn, S. A., Sharp, Z. D., et al. (2017). Incipient rifting accompanied by the release of subcontinental lithospheric mantle volatiles in the Magadi and Natron basin, East Africa. *Journal of Volcanology and Geothermal Research*, 346, 118–133. <https://doi.org/10.1016/j.jvolgeores.2017.03.017>
- Lee, H., Muirhead, J. D., Fischer, T. P., Ebinger, C. J., Kattenhorn, S. A., Sharp, Z. D., & Kianji, G. (2016). Massive and prolonged deep carbon emissions associated with continental rifting. *Nature Geoscience*, 9(2), 145–149. <https://doi.org/10.1038/ngeo2622>
- Lloyd, R., Biggs, J., Birhanu, Y., Wilks, M., Gottsmann, J., Kendall, J. M., et al. (2018a). Sustained Uplift at a Continental Rift Caldera. *Journal of Geophysical Research: Solid Earth*, 123(6), 5209–5226. <https://doi.org/10.1029/2018JB015711>
- Lloyd, R., Biggs, J., Wilks, M., Nowacki, A., Kendall, J. M., Ayele, A., et al. (2018b). Evidence for cross rift structural controls on deformation and seismicity at a continental rift caldera. *Earth and Planetary Science Letters*, 487, 190–200. <https://doi.org/10.1016/j.epsl.2018.01.037>
- Macpherson, C., & Matthey, D. (1994). Carbon isotope variations of CO₂ in Central Lau Basin basalts and ferrobasalts. *Earth and Planetary Science Letters*, 121(3–4), 263–276. [https://doi.org/10.1016/0012-821x\(94\)90072-8](https://doi.org/10.1016/0012-821x(94)90072-8)
- Marco, T., Barbara, N., Orlando, V., Santiago, M., Diego, M., & Alberto, R. (2021). Geothermics n de Soil CO₂ flux and temperature from a new geothermal area in the Cord o Inacaliri Volcanic Complex (northern Chile). *Geothermics*, 89(June 2020), 101961. <https://doi.org/10.1016/j.geothermics.2020.101961>
- Mazot, A., Rouwet, D., Taran, Y., Inguaggiato, S., & Varley, N. (2011). CO₂ and He degassing at El Chichón volcano, Chiapas, Mexico: Gas flux, origin and relationship with local and regional tectonics. *Bulletin of Volcanology*, 73(4), 423–441. <https://doi.org/10.1007/s00445-010-0443-y>
- Mazzarini, F., Rooney, T. O., & Isola, I. (2013). The intimate relationship between strain and magmatism: A numerical treatment of clustered monogenetic fields in the Main Ethiopian Rift. *Tectonics*, 32(1), 49–64. <https://doi.org/10.1029/2012tc003146>
- Mielnick, P. C., & Dugas, W. A. (2000). Soil CO₂ flux in a tallgrass prairie. *Soil Biology and Biochemistry*, 32(2), 221–228. [https://doi.org/10.1016/S0038-0717\(99\)00150-9](https://doi.org/10.1016/S0038-0717(99)00150-9)
- Minissale, A., Corti, G., Tassi, F., Darrah, T. H., Vaselli, O., Montanari, D., et al. (2017). Geothermal potential and origin of natural thermal fluids in the northern Lake Abaya area, Main Ethiopian Rift, East Africa. *Journal of Volcanology and Geothermal Research*, 336, 1–18. <https://doi.org/10.1016/j.jvolgeores.2017.01.012>
- Mohr, P. A. (1967). Major volcano–tectonic lineament in the Ethiopian rift system. *Nature*, 213(5077), 664–665. <https://doi.org/10.1038/213664a0>
- Mtili, K. M., Byrne, D. J., Tyne, R. L., Kazimoto, E. O., Kimani, C. N., Kasanzu, C. H., et al. (2021). The origin of high helium concentrations in the gas fields of southwestern Tanzania. *Chemical Geology*, 585(July), 120542. <https://doi.org/10.1016/j.chemgeo.2021.120542>
- Muirhead, J. D., Fischer, T. P., Oliva, S. J., Laizer, A., van Wijk, J., Currie, C. A., et al. (2020). Displaced cratonic mantle concentrates deep carbon during continental rifting. *Nature*, 582(7810), 67–72. <https://doi.org/10.1038/s41586-020-2328-3>
- Muirhead, J. D., Kattenhorn, S. A., Lee, H., Mana, S., Turrin, B. D., Fischer, T. P., et al. (2016). Evolution of upper crustal faulting assisted by magmatic volatile release during early-stage continental rift development in the East African Rift. *Geosphere*, 12(6), 1670–1700. <https://doi.org/10.1130/GES01375.1>
- Mulibo, G. D., & Nyblade, A. A. (2013). The P and S wave velocity structure of the mantle beneath eastern Africa and the African superplume anomaly. *Geochemistry, Geophysics, Geosystems*, 14(8), 2696–2715. <https://doi.org/10.1002/ggge.20150>
- Notsu, K., Sugiyama, K., Hosoe, M., Uemura, A., Shimoike, Y., Tsunomori, F., et al. (2005). Diffuse CO₂ efflux from Iwojima volcano, Izu-Ogasawara arc, Japan. *Journal of Volcanology and Geothermal Research*, 139(3–4), 147–161. <https://doi.org/10.1016/j.jvolgeores.2004.08.003>
- Nowacki, A., Wilks, M., Kendall, J. M., Biggs, J., & Ayele, A. (2018). Characterising hydrothermal fluid pathways beneath Aluto volcano, Main Ethiopian Rift, using shear wave splitting. *Journal of Volcanology and Geothermal Research*, 356, 331–341. <https://doi.org/10.1016/j.jvolgeores.2018.03.023>

- Ogden, C. S., Keir, D., Bastow, I. D., Ayele, A., Marcou, S., Ugo, F., et al. (2021). Seismicity and crustal structure of the southern Main Ethiopian Rift: New evidence from lake Abaya. *Geochemistry, Geophysics, Geosystems*, 22(8), 1–17. <https://doi.org/10.1029/2021GC009831>
- Omenda, P. A. (1998). The geology and structural controls of the Olkaria geothermal system, Kenya. *Geothermics*, 27(1), 55–74. [https://doi.org/10.1016/S0375-6505\(97\)00028-X](https://doi.org/10.1016/S0375-6505(97)00028-X)
- Ozima, M., & Podosek, F. A. (2002). *Noble gas geochemistry*. Cambridge University Press.
- Padrón, E., Hernández, P. A., Toulkeridis, T., Pérez, N. M., Marrero, R., Melián, G., et al. (2008). Diffuse CO₂ emission rate from Pululahua and the lake-filled Cuicocha calderas, Ecuador. *Journal of Volcanology and Geothermal Research*, 176(1), 163–169. <https://doi.org/10.1016/j.jvolgeores.2007.11.023>
- Pantaleo, M., & Walter, T. R. (2014). The ring-shaped thermal field of Stefanos crater, Nisyros Island: A conceptual model. *Solid Earth*, 5(1), 183–198. <https://doi.org/10.5194/se-5-183-2014>
- Parkinson, K. J. (1981). An improved method for measuring soil respiration in the field. *Journal of Applied Ecology*, 18(1), 221. <https://doi.org/10.2307/2402491>
- Parks, M. M., Caliro, S., Chiodini, G., Pyle, D. M., Mather, T. A., Berlo, K., et al. (2013). Distinguishing contributions to diffuse CO₂ emissions in volcanic areas from magmatic degassing and thermal decarbonation using soil gas ²²²Rn-δ¹³C systematics: Application to Santorini volcano, Greece. *Earth and Planetary Science Letters*, 377–378, 180–190. <https://doi.org/10.1016/j.epsl.2013.06.046>
- Peccerillo, A., Barberio, M. R., Yirgu, G., Ayalew, D., Barbieri, M., & Wu, T. W. (2003). Relationships between mafic and peralkaline silicic magmatism in continental rift settings: A petrological, geochemical and isotopic study of the Gedemsa volcano, Central Ethiopian rift. *Journal of Petrology*, 44(11), 2003–2032. <https://doi.org/10.1093/ptrology/egg068>
- Person, M., Hofstra, A., Sweetkind, D., Stone, W., Cohen, D., Gable, C. W., & Banerjee, A. (2012). Analytical and numerical models of hydrothermal fluid flow at fault intersections. *Geofluids*, 12(4), 312–326. <https://doi.org/10.1111/gfl.12002>
- Philippon, M., Corti, G., Sani, F., Bonini, M., Balestrieri, M. L., Molin, P., et al. (2014). Evolution, distribution, and characteristics of rifting in southern Ethiopia. *Tectonics*, 33(4), 485–508. <https://doi.org/10.1002/2013TC003430>
- Pürschel, M., Gloaguen, R., & Stadler, S. (2013). Geothermal activities in the Main Ethiopian Rift: Hydrogeochemical characterization of geothermal waters and geothermometry applications (Dofan-Fantale, Gerged-Sodere, Aluto-Langano). *Geothermics*, 47, 1–12. <https://doi.org/10.1016/j.geothermics.2013.01.001>
- Rango, T., Petrini, R., Stenni, B., Bianchini, G., Slejko, F., Beccaluva, L., & Ayenew, T. (2010). The dynamics of central Main Ethiopian Rift waters: Evidence from δD, δ¹⁸O and ⁸⁷Sr/⁸⁶Sr ratios. *Applied Geochemistry*, 25(12), 1860–1871. <https://doi.org/10.1016/j.apgeochem.2010.10.001>
- Remy, N., Boucher, A., & Wu, J. (2009). *Applied geostatistics with SGeMS: A user's guide*. Cambridge University Press.
- Rey, A., Pegoraro, E., Tedeschi, V., De Parri, I., Jarvis, P. G., & Valentini, R. (2002). Annual variation in soil respiration and its components in a coppice oak forest in Central Italy. *Global Change Biology*, 8(9), 851–866. <https://doi.org/10.1046/j.1365-2486.2002.00521.x>
- Ritsema, J., Deuss, A., Van Heijst, H. J., & Woodhouse, J. H. (2011). S40RTS: A degree-40 shear-velocity model for the mantle from new Rayleigh wave dispersion, teleseismic traveltime and normal-mode splitting function measurements. *Geophysical Journal International*, 184(3), 1223–1236. <https://doi.org/10.1111/j.1365-246x.2010.04884.x>
- Ritsema, J., Heijst, H. J. V., & Woodhouse, J. H. (1999). Complex shear wave velocity structure imaged beneath Africa and Iceland. *Science*, 286(5446), 1925–1928. <https://doi.org/10.1126/science.286.5446.1925>
- Robertson, E., Biggs, J., Edmonds, M., Clor, L., Fischer, T. P., Vye-Brown, C., et al. (2016). Diffuse degassing at Longonot volcano, Kenya: Implications for CO₂ flux in continental rifts. *Journal of Volcanology and Geothermal Research*, 327, 208–222. <https://doi.org/10.1016/j.jvolgeores.2016.06.016>
- Robertson, E. A. M., Biggs, J., Cashman, K. V., Floyd, M. A., & Vye-Brown, C. (2016). Influence of regional tectonics and pre-existing structures on the formation of elliptical calderas in the Kenyan Rift. *Geological Society Special Publication*, 420(1), 43–67. <https://doi.org/10.1144/SP420.12>
- Rooney, T. O., Bastow, I. D., & Keir, D. (2011). Insights into extensional processes during magma assisted rifting: Evidence from aligned scoria cones. *Journal of Volcanology and Geothermal Research*, 201(1–4), 83–96. <https://doi.org/10.1016/j.jvolgeores.2010.07.019>
- Rooney, T. O., Hanan, B. B., Graham, D. W., Furman, T., Blichert-toft, J., & Schilling, J. G. (2012). Upper mantle pollution during Afar plume-continental rift interaction. *Journal of Petrology*, 53(2), 365–389. <https://doi.org/10.1093/ptrology/egr065>
- Rooney, T. O., Hart, W. K., Hall, C. M., Ayalew, D., Ghiorsio, M. S., Hidalgo, P., & Yirgu, G. (2012). Peralkaline magma evolution and the tephra record in the Ethiopian Rift. *Contributions to Mineralogy and Petrology*, 164(3), 407–426. <https://doi.org/10.1007/s00410-012-0744-6>
- Salazar, J. M. L., Hernández, P. A., Pérez, N. M., Melián, G., Álvarez, J., Segura, F., & Notsu, K. (2001). Diffuse emission of carbon dioxide from Cerro Negro volcano, Nicaragua, Central America. *Geophysical Research Letters*, 28(22), 4275–4278. <https://doi.org/10.1029/2001GL013709>
- Samrock, F., Grayver, A. V., Eysteinnsson, H., & Saar, M. O. (2018). Magnetotelluric image of transcrustal magmatic system beneath the Tulu Moye geothermal prospect in the Ethiopian Rift. *Geophysical Research Letters*, 45(23), 12847–12855. <https://doi.org/10.1029/2018GL080333>
- Samrock, F., Kuvshinov, A., Bakker, J., Jackson, A., & Fisseha, S. (2015). 3-D analysis and interpretation of magnetotelluric data from the Aluto-Langano geothermal field, Ethiopia. *Geophysical Journal International*, 202(3), 1923–1948. <https://doi.org/10.1093/gji/ggv270>
- Sano, Y., & Marty, B. (1995). Origin of carbon in fumarolic gas from island arcs. *Chemical Geology*, 119(1–4), 265–274. [https://doi.org/10.1016/0009-2541\(94\)00097-r](https://doi.org/10.1016/0009-2541(94)00097-r)
- Saria, E., Calais, E., Stamps, D. S., Delvaux, D., & Hartnady, C. J. H. (2014). Present-day kinematics of the East African Rift. *Journal of Geophysical Research: Solid Earth*, 119(4), 3584–3600. <https://doi.org/10.1002/2013JB010901>
- Schöpa, A., Pantaleo, M., & Walter, T. R. (2011). Scale-dependent location of hydrothermal vents: Stress field models and infrared field observations on the Fossa Cone, Vulcano Island, Italy. *Journal of Volcanology and Geothermal Research*, 203(3–4), 133–145. <https://doi.org/10.1016/j.jvolgeores.2011.03.008>
- Shimoike, Y., Kazahaya, K., & Shinohara, H. (2002). Soil gas emission of volcanic CO₂ at Satsuma-Iwojima volcano, Japan. *Earth Planets and Space*, 54(3), 239–247. <https://doi.org/10.1186/BF03353023>
- Sierra, D., Hidalgo, S., Almeida, M., Vigide, N., Lamberti, M. C., Proaño, A., & Narváez, D. F. (2021). Temporal and spatial variations of CO₂ diffuse volcanic degassing on Cuicocha Caldera Lake–Ecuador. *Journal of Volcanology and Geothermal Research*, 411, 107145. <https://doi.org/10.1016/j.jvolgeores.2020.107145>
- Simiyu, S. M., & Keller, G. R. (2000). Seismic monitoring of the Olkaria Geothermal area, Kenya Rift valley. *Journal of Volcanology and Geothermal Research*, 95(1–4), 197–208. [https://doi.org/10.1016/S0377-0273\(99\)00124-9](https://doi.org/10.1016/S0377-0273(99)00124-9)
- Sinclair, A. J. (1974). Selection of threshold values in geochemical data using probability graphs. *Journal of Geochemical Exploration*, 3(2), 129–149. [https://doi.org/10.1016/0375-6742\(74\)90030-2](https://doi.org/10.1016/0375-6742(74)90030-2)
- Sperrevik, S., Gillespie, P. A., Fisher, Q. J., Halvorsen, T., & Knipe, R. J. (2002). Empirical estimation of fault rock properties. In *Norwegian petroleum society special publications* (Vol. 11, pp. 109–125). Elsevier.

- Tassi, F., Vaselli, O., Papazachos, C. B., Giannini, L., Chiodini, G., Vougioukalakis, G. E., et al. (2013). Geochemical and isotopic changes in the fumarolic and submerged gas discharges during the 2011–2012 unrest at Santorini caldera (Greece). *Bulletin of Volcanology*, *75*(4), 1–15. <https://doi.org/10.1007/s00445-013-0711-8>
- Tedesco, D., Tassi, F., Vaselli, O., Poreda, R. J., Darrah, T., Cuoco, E., & Yalire, M. M. (2010). Gas isotopic signatures (He, C, and Ar) in the Lake Kivu region (western branch of the East African rift system): Geodynamic and volcanological implications. *Journal of Geophysical Research*, *115*(1), 1–12. <https://doi.org/10.1029/2008JB006227>
- Temtime, T., Biggs, J., Lewi, E., Hamling, I., Wright, T., & Ayele, A. (2018). Spatial and temporal patterns of deformation at the Tendaho geothermal prospect, Ethiopia. *Journal of Volcanology and Geothermal Research*, *357*, 56–67. <https://doi.org/10.1016/j.jvolgeores.2018.04.004>
- Tierz, P., Clarke, B., Calder, E. S., Dessalegn, F., Lewi, E., Yirgu, G., et al. (2020). Event trees and epistemic uncertainty in long-term volcanic hazard assessment of rift volcanoes: The example of Aluto (Central Ethiopia). *Geochemistry, Geophysics, Geosystems*, *21*(10), e2020GC009219. <https://doi.org/10.1029/2020GC009219>
- Viveiros, F., Cardellini, C., Ferreira, T., Caliro, S., Chiodini, G., & Silva, C. (2010). Soil CO₂ emissions at Furnas volcano, São Miguel Island, Azores archipelago: Volcano monitoring perspectives, geomorphologic studies, and land use planning application. *Journal of Geophysical Research*, *115*(12), 1–17. <https://doi.org/10.1029/2010JB007555>
- Weiss, R. F. (1968). Piggyback sampler for dissolved gas studies on sealed water samples. In *Deep sea research and oceanographic abstracts* (Vol. 15, pp. 695–699). Elsevier.
- Werner, C., Brantley, S. L., & Boomer, K. (2000). CO₂ emissions related to the Yellowstone volcanic system 2. Statistical sampling, total degassing, and transport mechanisms. *Journal of Geophysical Research*, *105*(B5), 10831–10846. <https://doi.org/10.1029/1999jb900331>
- Werner, C., & Cardellini, C. (2006). Comparison of carbon dioxide emissions with fluid upflow, chemistry, and geologic structures at the Rotorua geothermal system, New Zealand. *Geothermics*, *35*(3), 221–238. <https://doi.org/10.1016/j.geothermics.2006.02.006>
- Werner, C., Hurwitz, S., Evans, W. C., Lowenstern, J. B., Bergfeld, D., Heasler, H., et al. (2008). Volatile emissions and gas geochemistry of Hot Spring Basin, Yellowstone National Park, USA. *Journal of Volcanology and Geothermal Research*, *178*(4), 751–762. <https://doi.org/10.1016/j.jvolgeores.2008.09.016>
- Wilks, M., Kendall, J. M., Nowacki, A., Biggs, J., Wookey, J., Birhanu, Y., et al. (2017). Seismicity associated with magmatism, faulting and hydrothermal circulation at Aluto Volcano, Main Ethiopian Rift. *Journal of Volcanology and Geothermal Research*, *340*, 52–67. <https://doi.org/10.1016/j.jvolgeores.2017.04.003>
- Wilks, M., Rawlinson, N., Kendall, J. M., Nowacki, A., Biggs, J., Ayele, A., & Wookey, J. (2020). The coupled magmatic and hydrothermal systems of the restless Aluto caldera, Ethiopia. *Frontiers of Earth Science*, *8*(October), 1–14. <https://doi.org/10.3389/feart.2020.579699>
- Wolfenden, E., Ebinger, C., Yirgu, G., Deino, A., & Ayalew, D. (2004). Evolution of the northern Main Ethiopian rift: Birth of a triple junction. *Earth and Planetary Science Letters*, *224*(1–2), 213–228. <https://doi.org/10.1016/j.epsl.2004.04.022>